

BATTERY CHARGE AND DISCHARGE CONTROL  
FOR ENERGY MANAGEMENT  
IN EDV AND UTILITY INTEGRATION

by

KE BAO

SHUHUI LI, COMMITTEE CHAIR

KEITH A. WILLIAMS  
JABER ABU QAHOUC

A THESIS

Submitted in partial fulfillment of the requirements  
for the degree of Master of Science in the  
Department of Electrical and Computer  
Engineering in the Graduate School of  
The University of Alabama

TUSCALOOSA, ALABAMA

2012

Copyright Ke Bao 2012  
ALL RIGHTS RESERVED

## ABSTRACT

Electric drive vehicles (EDVs) have many benefits as compared to normal petrol or gas cars. Moreover, the electrification of transportation systems would enable increased electricity generation from carbon-free and renewable energy sources, such as wind, solar, and hydro. However, due to highly distributed and mobile nature as well as high charge and discharge power demand of EDVs, it is important to investigate how to manage EDV charge and discharge to enhance the usage of renewable enough resources in the future smart grid framework.

For this purpose, this thesis first investigates typical battery electrochemical properties which are important concerns for the design of EDV charge and discharge. In this section, mathematical and circuit-oriented battery models are investigated to reflect typical battery electrochemical properties. Meanwhile, the relation between mathematical and circuit-oriented battery models is analyzed.

Then, this thesis presents an energy control study in a charging station, a typical integrated EDV and utility system. The charging station consists of an AC/DC converter for grid interface and multiple dc/dc converters for EDV battery management. For the grid-side converter, a direct-current control mechanism is employed for reactive power, ac system bus voltage, and DC-link voltage control. For the EDV-side converters, constant-current and constant-voltage control mechanisms are investigated for charging and discharging control. The thesis considers energy management need for charge and discharge of multiple EDVs simultaneously as well as energy transferring from vehicle to grid and grid to vehicle requirements. A real-time simulation

model is investigated and the performance of the integrated EDV and utility system is investigated.

## LIST OF ABBREVIATIONS AND SYMBOLS

<i>V</i>	Volts: Unit of voltage.
<i>A</i>	Amperes: Unit of current.
<i>kW</i>	kilo Watts: Unit of active power.
<i>kVar</i>	kilo Vars: Unit of reactive power.
<i>Hz</i>	Hertz: Unit of frequency
<i>DC</i>	Direct current
<i>AC</i>	Alternative current
<i>MOSFETs</i>	MOS Field Effect Transistors
<i>GTOs</i>	Gate Turn Off Thyristors
<i>IGBTs</i>	Insulated Gate Bipolar Transistors
<i>PID</i>	Proportional-integral-derivative
<i>GSC</i>	Grid side converter
<i>ESC</i>	EDVs side converter
<i>OCV</i>	Open circuit voltage
<i>SOC</i>	State of charge
<i>DOD</i>	Depth of discharge
<i>ICE</i>	Internal combustion engine
<i>V2G</i>	Vehicle to grid
<i>G2V</i>	Grid to vehicle

## **ACKNOWLEDGMENTS**

I would like to personally thank the following people who support me with my sincere gratitude. First and foremost, I would like to show my deepest gratitude to my supervisor, Dr. Shuhui Li, a respectable, responsible and resourceful scholar, who has provided me with valuable guidance in every stage of the writing of this thesis. Without his enlightening instruction, impressive kindness and patience, I could not have completed my thesis. His keen and vigorous academic observation enlightens me not only in this thesis but also in my future study.

I would also like to thank all my teachers who have helped me to develop the fundamental and essential academic competence. My sincere appreciation also goes to my schoolmates from ECE department in university of Alabama, who participated this study with great cooperation.

This research would not have been possible without the support of them and of course of my family who never stopped encouraging me to persist. Finally I thank all of them again for their encouragement and support.

## CONTENTS

ABSTRACT.....	ii
LIST OF ABBREVIATIONS AND SYMBOLS .....	iv
ACKNOWLEDGMENTS .....	v
LIST OF FIGURES .....	xi
1. INTRODUCTION .....	1
1.1 Summary of EDVs.....	1
1.2 Energy storage system of EDVs .....	3
1.3 Charging strategy of the EDVs.....	4
1.4 Purpose of the Thesis.....	5
2. OVERVIEW OF BATTERY ENERGY MANAGEMENT IN EDV AND ELECTRIC UTILITY INTEGRATION.....	6
2.1 Batteries in EDVs and electric power grid .....	6
2.2 Configuration of grid connected EDVs charging station.....	8
2.3 Dynamic electric price and V2G, G2V, V2V functions .....	10
3. REVIEW OF BATTERY MODELING USING MATHEMATICAL AND CIRCUIT ORIENTED APPROACHES.....	13
3.1 Introduction of battery modeling .....	13
3.2 Battery characteristics for model development.....	15
3.2.1 Electrochemical cell.....	15
3.2.2 Current flow and polarization .....	16
3.2.3 Other factors affecting batteries.....	17

3.2 Battery characteristics for model development.....	15
3.2.1 Electrochemical cell.....	15
3.2.2 Current flow and polarization .....	16
3.3. Mathematical battery models.....	18
3.4. Circuit-Oriented battery models .....	21
3.5. Parameter extraction for mathematical and circuit-oriented battery Models.....	25
3.5.1 Other factors affecting battery models.....	25
3.5.2 Parameter extraction of circuit-oriented battery model .....	26
3.6. Parameter extraction for mathematical and circuit-oriented battery Models.....	28
3.6.1 Shepherd discharge model under simple parameter extraction strategy .....	29
3.6.2 Modified shepherd model under simple parameter extraction strategy .....	31
3.6.3 Parameter extraction by linear regression.....	33
3.6.4 Modified shepherd charge model.....	34
3.7 Conclusions.....	36
4. GRID-SIDE CHARGER CIRCUIT CONFIGURATUON OF EDVs CHARGING STATION.....	38
4.1 Topology of EDVs charging infrastructure in grid side system .....	38
4.2 Grid-side converter (GSC).....	39
4.3 LCL filter design.....	41
4.4 Pre-charging strategy .....	46

4.5 Vector control in d-q reference frame theory .....	48
4.5.1 Space vectors definition.....	48
4.5.2 Grid-side converter system schematic .....	51
4.5.3 Real power and reactive power of the grid side system.....	52
4.6 Purposed current loop control strategy .....	53
4.6.1 Inner current control loop .....	53
4.6.2 DC-Link voltage control loop.....	54
4.6.3 Overall direct-current loop control strategy in grid side system.....	55
5. EDVs SIDE CHARGER CIRCUIT CONGIGURATUON OF THE CHARGING STATON.....	58
5.1 Battery charging and discharging characteristic .....	58
5.1.1 Charging requirement .....	59
5.1.2 Discharging scheme .....	60
5.2 Structure of EDVs side system .....	61
5.2.1 DC-DC converter structure .....	62
5.2.2 LCL filter in EDV side system .....	63
5.3 EDV side control scheme.....	66
6. REAL TIME SIMULATION IMPLEMENTATION.....	68
6.1 Introduction of Real-time simulation.....	68
6.2 Functions of Real-time simulations .....	68
6.3 Time-step in real-time simulation.....	70

6.4 RT-LAB for real-time simulation .....	72
6.4.1 ARTEMiS toolbox .....	72
6.4.2 RT-Events toolbox .....	73
6.4.3 From Simulink based design to Real-Time module by RT-Lab.....	74
6.5 Computational Experiment System of EDVs Charging Station for Real-Time Simulation .....	78
6.6 Grid side system module of the integrated EDVs charging system.....	81
6.6.1 Module for three-phase axes to $dq$ -axes frame reference transformation .....	81
6.6.2 Directed-current control modules for GSC .....	82
6.7 EDVs side system module of the integrated EDVs charging system ....	83
6.7.1 EDVs side power path module .....	83
6.7.2 EDVs side control system.....	84
7. EDV CHARGING STATION CONTROL EVALUATION IN TRANSIENT CLOSE-LOOP ENVIRONMENT .....	86
7.1 Reactive Power Control and PCC Voltage Compensation in Grid Side System .....	86
7.1.1 Charge/Discharge and Grid Reactive Power Controls.....	86
7.1.2 Charge/Discharge and Grid Voltage Support Controls .....	89
7.2 G2V, V2G and V2V simulation.....	91
7.2.1 G2V model simulation .....	91
7.2.2 V2G model simulation.....	94
7.2.3 V2V model simulation.....	96
7.3 Conclusions.....	97

8. SUMMARY AND FUTURE WORK .....	98
9. REFERENCES .....	100

## LIST OF FIGURES

2.1. EDV charging kit in the central park of New York .....	8
2.2. Configuration of Grid Connected EDVs Charging Infrastructure .....	9
2.3. Grid Connected EDVs Charging Infrastructure with AC Bus.....	10
2.4. SEC dynamic electricity price during different seasons and days .....	12
3.1. Schematic representation of the operation of electrochemical cell ....	16
3.2. Typical battery discharge curve .....	19
3.3. Mathematical flow chart of a battery model .....	21
3.4. Circuit-oriented battery models .....	23
3.5. Performance of Shepherd model for a lead-acid battery .....	29
3.6. Performance of modified Shepherd model for a lead-acid battery .....	32
3.7. Comparison between model prediction and measurement for a lead-acid battery using linear regression method.....	35
3.8. Comparison between model prediction and measurement when the parameters used for charge and discharge models are the same .....	36
4.1. Configuration of grid side system for EVs charging infrastructure....	39
4.2. A conventional AC/DC converter.....	41
4.3 Equivalent single-phase LCL filter at the h harmonic .....	42
4.4 Current ripple at the beginning of the charging process .....	47
4.5. Complex stator current vector and the component in (a, b, c).....	48
4.6 Clarke transformation .....	49
4.7. d-q rotating reference frame obtained by Park Transformation.....	50

4.8 Grid-side converter system .....	51
4.9 Inner current loop control .....	54
4.10 The DC-Link voltage loop control scheme.....	55
4.11 Direct-current vector control structure.....	56
5.1 EV side system structure of EVs charging system .....	62
5.2 DC-DC buck-boost converter .....	63
5.3 Constant-current and constant-voltage control mechanisms for charging and discharging of EV battery.....	66
6.1 Fixed time step simulation .....	70
6.2 overrun phenomenon in real time simulation .....	71
6.3 Comparison between RT-Event and Standard Simulink .....	74
6.4. Interface of RT-LAB software.....	75
6.5 Status of different kinds of subsystems for RT-LAB .....	76
6.6 Maximum parallel execution by “integrator” or “memory” blocks.....	77
6.7 Interface for configuration parameters in RT-LAB .....	78
6.8 Real-time simulation structure of converter system for EDV charging station .....	80
6.9 Module for three-phase axes to dq axes frame reference transformation .....	82
6.10 Directed-current control module.....	82
6.11 Vd1 and Vq1 signals generation blocks in proposed control system	83
6.12 EDVs side control system module .....	85

# CHAPTER 1

## INTRODUCTION

### 1.1 Summary of EDVs

Due to the plentiful consumption of gasoline and exhaust of the greenhouse gases, some environmental problems, such as global warming and non-renewable resources + have become a critical problem which has attracted much attention from the whole world. Regarding transportation, vehicles not only consumed voluminous fossil fuel, but also released numerous greenhouse gases to the atmosphere. For this fact, a number of research institutions and automobile companies have gradually devoted their interests on researching and developing alternative energy resource to replace or restrict the gasoline consumption in conventional vehicles. As a substitute of conventional vehicles, Electric Drive Vehicles (EDVs) have gradually been accepted by the public in past decades. According to reference [1], Hybrid electric vehicle sales in the United States have grown from 9,367 in 2000 to 324,318 through 2007.

The term EDV has actually come to include several different vehicle technologies [7]. The main types available today are listed below.

1. Hybrid electric vehicles (HEVs): A HEV is a type of hybrid vehicle and electric vehicle which combines a conventional internal combustion engine propulsion system with an electric propulsion system. The presence of the electric powertrain is intended to achieve either better fuel economy than a conventional vehicle, or better

performance. Modern HEVs make use of efficiency-improving technologies such as regenerative braking, which converts the vehicle's kinetic energy into electric energy to charge the battery, rather than wasting it as heat energy as conventional brakes do.

2. Electric vehicles (EVs): an EV uses one or more electric motors or traction motors for propulsion. Besides the capability of reusing the vehicle's kinetic energy to charge the battery as a HEV, an EV can also be powered by charging from external power source.
3. Plug-in Hybrid Electric Vehicles (PHEVs): a PHEV is a hybrid vehicle which utilizes rechargeable batteries, or another energy storage device, that can be restored to full charge by connecting a plug to an external electric power source (usually a normal electric wall socket). A PHEV shares the characteristics of both a conventional hybrid electric vehicle, namely, having an electric motor and an internal combustion engine (ICE)

In fact, HEVs are the only type of EDVs which have been largely sold on the market in the past years. Due to the past technical restriction, the battery in a HEV was designed in a very small capability and is merely used to store energy from the kinetic energy. However, it has already been confirmed by the HEVs customers that this improvement dramatically increase gasoline efficiency and reduce exhaust emission comparing with conventional vehicles. [1] Therefore, it is reasonable to believe that the PHEVs and EVs, which are seen as the next generation of EDVs, will provide a much better energy efficiency and performance than HEVs. Referring to IEEE-USA's Energy Policy Committee, "a PHEV is designed to possess following characteristics [2]: (1) a PHEV needs to be equipped with a battery storage system with the capability of 4kWh or more, which is used to power the motion of the vehicle; (2) the battery

system of a PHEV is able to be charged from an external source of electricity; and (3) the least driving distance of a PHEV has to be more than 10 miles (16.1km) in all-electric mode consuming without gasoline”. Referring to the characteristics listed above, the 10 miles minimum all-electric mode driving distance for a PHEV is the most dominant point than HEVs, since the 10 miles is long enough to satisfy the daily commuting distance to most people. Therefore, the gasoline consumption can be minimized into an impressive extent by the utilization of PHEVs. In the EVs case, it totally gets rid of ICE through a more powerful electric power storage device and electromotor than PHEVs. Due to current technical obstacles, such as energy storage device efficiency, capacity and life cycle, EVs confront more severe technical challenges than PHEVs. Since EVs can completely avoid the consumption of gasoline and can be fully charged by external electric source, EVs are seen as the update of PHEVs in the future.

## **1.2 Energy storage system of EDVs**

The electrical energy storage system in the EVs, HEVs and PHEV is expected to be designed with sufficient energy capacity and adequate output peak power to satisfy real-world vehicle driving and acceleration performance [3]. In addition, adequate cycle and calendar longevity of an energy storage system also play crucial roles in the performance of a PHEV or EV. Although the requirements of the energy storage units vary significantly depending on the various EDVs, it is certain that EDVs have brought severer challenges on the energy storage device than other applications. Regarding this fact, a common problem is presented that it is difficult to store a mass of electrical energy in an economical and efficient way. Capacitors are able to directly store electricity, but the quantities are small. Thus, the storage of electrical energy requires its conversion into another form of energy. A battery is a device that can store

the electrical energy into chemical energy and release the energy by chemical reaction when it is needed [4, 5].

From EDVs perspectives, a battery system is used to store the electric energy by vehicle regenerative braking or charged from external generator plant. Depending on the type of EDVs, the standard of a battery system is variable in many aspects, such as materials, size, weight, capability etc. The size of a PHEV battery system is supposed to be smaller than an EV battery, since the less electric energy is demanded by a PHEV than EV. Meanwhile, a deep charging ability and long cycle life battery is necessary in a PHEV rather than shallow discharging battery in a HEV. Moreover, a PHEV battery has to possess a high energy density and high power output as well as long life cycle to obtain an acceptable acceleration and driving distance. At present, two types of high efficient batteries, nickel metal hydride battery and Lithium-ion battery are seen as the most prevalent in the PHEVs and EVs case.

### **1.3 Charging strategy of the EDVs**

The conventional three charging levels were defined by the Electric Power Research Institute and codified in the National Electric along with corresponding functionality requirements and safety systems [1]. First, with 120V voltage and 20A current electricity standard, the AC level 1 charging scheme is the slowest charging scheme of the 3 levels. Normally, the level 1 charging scheme may spend more than 8 hours to fill a large capacity battery pack such as 10kWh. Moreover, the charger of the level 1 scheme is so simple that the charging equipment can be incorporated on the vehicle, which enables the charging process at any household power source. A 240V, 30A branch circuit is utilized by level 2 AC charging scheme. This single-phase charging issue possesses a higher charging speed and more expensive charging equipment than level 1. However, it still needs to take hours to charge a high capacity

EDV battery for level 2 charging scheme. Therefore, both level 1 and level 2 schemes are supposed to be utilized in overnight charging at a home garage or an apartment complex. The Level 3 DC charging method is the fastest charging scheme of 3 levels with a 480V three phases branch circuit. Theoretically, the PHEV or EDV battery can get 50% energy in 10-15 minutes by this charging level. [2] With this charging rate, the level 3 charging scheme can provide EDV customers the refueling experience which is same as the current gas station provide. Differing from the level 1 and level 2 schemes, the fast charging rate requires a much higher level power supplement in the charging process, which cannot be afforded by the domestic electricity supplies. Therefore, it is necessary to establish a grid integrated electric vehicle charging station for the level 3 fast charging process achievement.

#### **1.4 Purpose of the Thesis**

The purpose of this thesis is to investigate battery charge and discharge control strategies for integrated utility and vehicle systems, such as EDV charging stations. In the chapter that follows, the thesis first presents overview of typical configuration of an integrated utility and vehicle system – a grid-connected EDV charging station in Chapter 2. Chapter 3 presents a comparison between a series battery modeling using mathematical and circuit oriented approaches. A direct-current control mechanism for the grid-side converter (GSC) is introduced in Chapter 4. Chapter 5 presents Control mechanisms of EDV-side converters (ESCs) for battery charge and discharge management. Chapter 6 shows a real-time simulation system for performance evaluation of the charging station. Simulation studies are provided in Chapter 7. Finally, the thesis concludes with the summary of the main points.

## **CHAPTER 2**

### **OVERVIEW OF BATTERY ENERGY MANAGEMENT IN EDV AND ELECTRIC UTILITY INTEGRATION**

As a result of fast improving of EDVs technology, it is expected that the electric utility and transportation systems in the U.S. will become increasingly integrated and indistinguishable from each other due to the electrification of the transportation system. One important issue for the integration of EDVs and utility system is the power control and management of EDV batteries.

#### **2.1 Batteries in EDVs and electric power grid**

Due to the high variability of energy production and consumption over time, a high capacity battery is to accommodate this energy production and consumption variability. During the time that energy production higher than the consumption, a battery can be charged to store the extra power. On the contrary, the battery can be discharged and send the stored energy into the grid to satisfy the demand of the grid during the peak load of the electrical power grid. In this way, electricity production of the conventional generators do not need to be drastically scaled up or down to meet the momentary consumption, which would increase efficiency and lower the

cost of energy production and facilitate the use of intermittent energy sources, such as photovoltaic and wind turbines [6].

On the other hand, a battery storage system is one of the most critical and expensive components for an EDV. Because of the chemical structure of an EDV battery in nature, the health of an EDV battery is influenced seriously by the internal and external environment. An improper charging or discharging process can easily shorten the life cycle and weaken the performance of the EDV battery. Empirically, recurring cost of EDVs such as battery replacement and charging equipment has been considered as a big burden for EDVs' customers. Especially for PHEVs and EVs, these two types of EDVs require deeper battery charging and discharging cycles than conventional hybrids. Concerning the negative impact of the deep charging and discharging cycles on life circle of an EDV battery, the battery life in PHEVs or EVs could be much less than the traditional HEVs. For these facts, a series of design issues, including charge/discharge control strategy and trade-offs against battery life, capacity, heat dissipation, weight, costs, and safety need to be considered in PHEVs and EVs applications. Particularly, the EDVs charging station in this thesis is intend to realize the level 3 fast charging experience as defined in SAE J1772 [2] and minimize the damage of the EDV batteries caused by the fast charge.

## 2.2 Configuration of grid connected EDVs charging station

A grid integrated EDVs charging station is an infrastructure that supplies electricity energy for recharging the PHEVs or EVs.

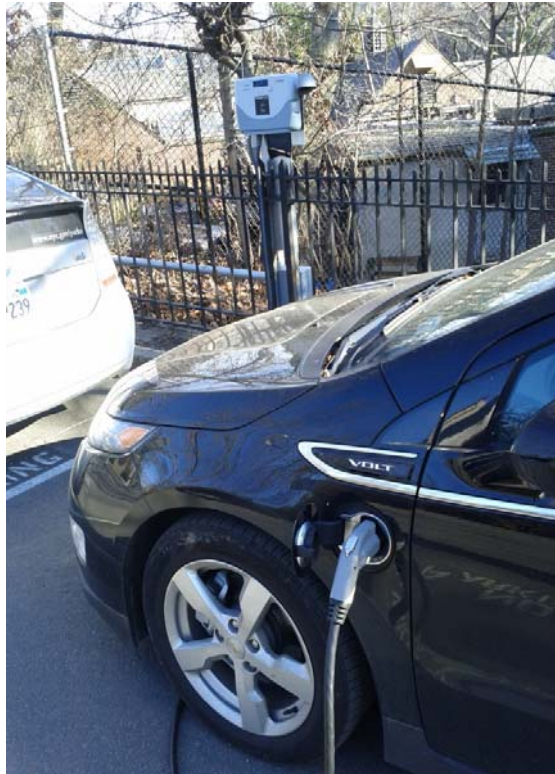


Fig. 2.1 EDV charging kit in the central park of New York

Accompanying the growing quantity of the PHEVs and EVs customers, the need of EDVs charging station is also unceasingly expanding in recent years. At present, most of charging stations are still established through domestic supplies, which aim to provide the level1 and level2 charging schemes to EDVs. Figure 2.1 shows a household supply based charging kit in the central park of New York. Although the level1 and level2 charging schemes can be easier equipped than the fast charging station with the advantages of low cost and wide compatibility

for most of the household power supplies, the charging time is still one of the factors that obstructs the popularization of PHEVs and EVs. Hence, a fast charging station with the fast charging and other functions is seen as a better solution for EDVs popularization in the future.

A grid integrated EDVs charging station for fast charging scheme mainly contains three parts: a series of EDVs, power electronic converters, and an integrated control system. [8] The power converting system consists of two types of the current-regulated voltage-source PWM converters, including a grid-side converter (GSC) and a range of EDV-side converters (ESCs) [8, 9]. As shown in figure 2.2, a DC-Link capacitor is combined with the grid side convertor (GSC) in the middle of the circuit for conversion between the three-phase voltage from the grid and DC voltage from the EDVs. The DC-bus links a range of EDVs and each of EDVs is equipped with a DC-DC converter. In the left part of the circuit, a three-phase LCL filter is introduced between the power grid and the GSC to get rid of the high order frequency oscillations.

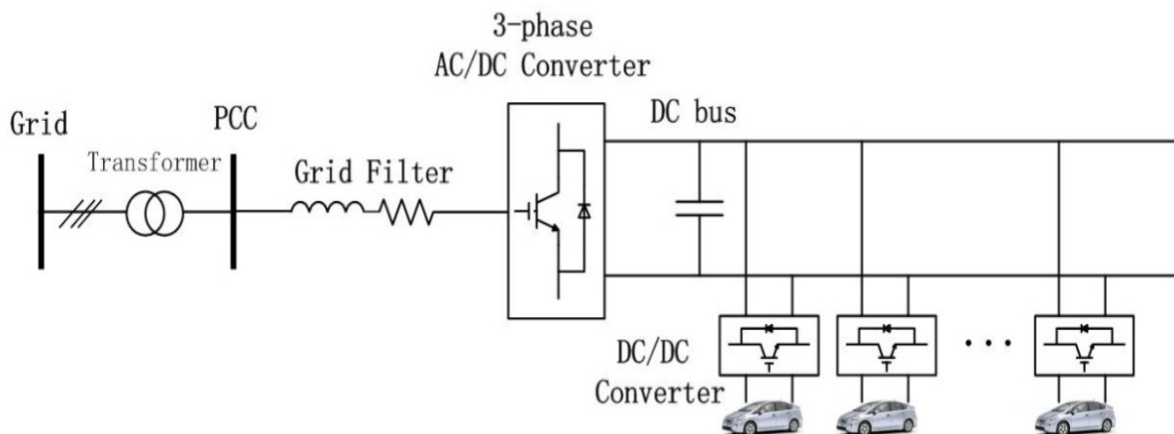


Fig. 2.2. Configuration of Grid Connected EDVs Charging Infrastructure

Comparing to the conventional AC bus architecture, the DC bus structure is more suitable for the purposed EDVs charging station. For the conventional AC bus based system, the AC bus is established by a transformer and each of power terminal customers is collocate with an AC-DC converter. To obtain the DC power, one more DC-DC converter is also equipped to terminal customers (figure 2.3). Actually, the AC system has been used for years and there are well developed standards and technologies available [7]. On the other hand, the DC bus architecture utilizes one high power 3-phase AC-DC converter instead of a number of AC-DC converters utilized in AC bus based architecture. Since most of renewable source and EDVs are interfaced to a common DC bus, this architecture provides a more convenient way to integrate the EDVs and the renewable energy generators. Moreover, less conversions of the DC bus architecture also enhance the efficiency and lower the cost of the station. Therefore, the DC bus based architecture is adopted in this thesis.

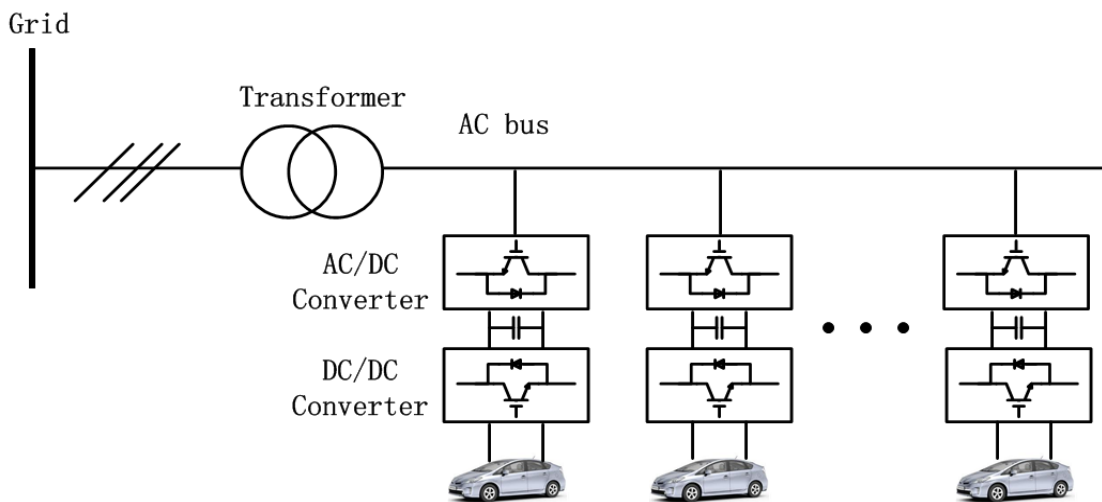


Fig. 1.3. Grid Connected EDVs Charging Infrastructure with AC Bus

### **2.3 Dynamic Electric Price and V2G, G2V, V2V Functions**

As mentioned before, the electricity is distinct with most kinds of traditional commodities in cost of production, because it is hardly stored economically. This fact means the demand for electricity plays a dominant role in the electricity market. Moreover, the electricity demand is so variable that the power demand is changing in hours every day. For these features of electricity, some of electricity capacity is putted in an idle position during the low ebb of demand moment, while the capacity is roped at the maximum level when a peak demand for electricity is on. About these two facts, the electricity price for peak demand is supposed much higher than low demand, because of influence from the relation between supply and demand. At the same time, the electricity price is also raised by the high cost of electricity generation when the grid is working at maximum capacity. As a result, the electricity price should be sold in dynamic price which fluctuates over time to reflect the real value of electricity caused by supply and demand. Instead of the conventional flat price rate structure, the dynamic electricity price could be considerably higher at certain time of the day and certain time of the year.

Currently, electric utility companies typically use hourly day-ahead real-time price (RTP) structure in their dynamic pricing program, in which hourly electricity prices for the entire next day are published day-ahead. Both Southern California Edison's (SCE's) and New York Con Edison's RTP tariffs are working on this application [10]. Figure 2.4 shows SCE's RTP tariff for five summer weekdays corresponding to different weather conditions (i.e., mild [ $<80^{\circ}\text{F}$ ], moderate [ $81^{\circ}\text{F}$ – $84^{\circ}\text{F}$ ], hot [ $85^{\circ}\text{F}$ – $90^{\circ}\text{F}$ ], very hot [ $91^{\circ}\text{F}$ – $94^{\circ}\text{F}$ ], and extremely hot [ $>95^{\circ}\text{F}$ ]), two

winter weekday conditions, and two summer and winter weekend conditions [10, 11]. The actual value of the electricity illustrated in this figure is dramatically variable during these testing weekdays. Especially in some hot days, it is impossible to accurately reflect the actual electricity price by the conventional flat price rate structure.

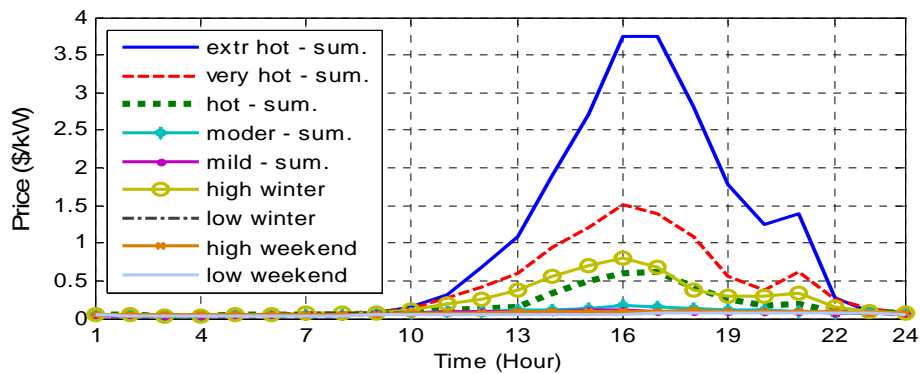


Fig. 2.4. SEC dynamic electricity price during different seasons and days

Due to the large variation of electricity price, developing G2V, V2G, and V2V functions has become the most fascinating capabilities of a EDVs charging station. For the G2V operating mode, the EDVs absorb power from the grid during the low demand period and the power flowing direction is from the grid to the EDVs at this moment. Depending on the specific situation, it is also possible that some EDVs are under charging mode while the other EDVs are being discharged. This process is called V2V mode and the power is transferred from the vehicles to other vehicles in this mode. For the V2G operating mode, the charging station supplies power to the grid. This function of the integrated charging station is particularly beneficial during the peak demand condition when the electricity price keeps in a high level.

## **CHAPTER 3**

### **REVIEW OF BATTERY MODELING USING MATHEMATICAL AND CIRCUIT ORIENTED APPROACHES**

#### **3.1 Introduction of Battery Modeling**

Because of the complex charging/discharging characteristics and relative damageable feature of battery, it is necessary to establish accurate battery models which can help the design of charging station more efficiently and reliably. Researchers around the world have developed a wide variety of battery models with varying degrees of complexity. The two primary modeling strategies are mathematical and circuit-oriented modeling strategies.

Traditionally, mathematical battery models [4-8] are developed based primarily on the Shepherd relation [10] to predict system-level behavior, such as battery runtime, efficiency, or capacity. But, most conventional mathematical battery models are considered to work only for specific applications and can provide inaccurate results in the order of 5%–20% error [9]. Many recent mathematical battery models are improved significantly by adding and modifying terms of traditional battery models to relax the assumptions behind the Shepherd model, which is considered to be able to represent the battery voltage dynamics more accurately when the current varies as well as when considering battery age, history and charge/discharge regimes.

Circuit-oriented battery models [9]–[18] are electrical equivalent models using a combination of voltage sources, resistors, and capacitors and are normally used by electrical engineers for co-design and co-simulation with other electrical circuits and systems. There have been many circuit-oriented battery models. Similar to the mathematical battery model development, circuit-oriented battery models have also gone through different stages from early low accuracy Thevenin-based [10]–[16] and impedance-based [17], [18] battery models to more accurate runtime-based RC network battery models developed recently [9], [19].

Due to the battery model development in the two different directions, it becomes important to investigate the relations, differences, and computational complexities using the two modeling approaches. This chapter first briefly reviews the electrochemical characteristics that are important for battery model development in Section 3.2. Section 3.3 presents mathematical battery models including a modified battery model based on MatLab SimPowerSystems. Section 3.4 shows typical circuit-based battery models and their relation with the mathematical battery models. Section 3.5 studies parameter extraction as well as computational complexity associated with the model extraction using the two different modeling approaches. Section 3.6 gives performance assessment of mathematical battery model for different charge and discharge applications.

## **3.2 Battery Characteristics for Model Development**

A rechargeable battery is one or more electrochemical cells that convert stored chemical energy into electrical energy during a discharge process or convert electrical energy into chemical energy during a charge process [20].

### **3.2.1 Electrochemical cell**

An electrochemical cell is a chemical device for generating or storing electric energy. It consists of a positive electrode and a negative electrode, separated by electrolyte (figure 3.1). The electrolyte is capable of conducting ions between the two electrodes, but is itself an electronic insulator. The positive and negative electrodes are immersed in the electrolyte and the reacting substances usually are stored within the electrodes, sometimes also in the electrolyte. The chemical reactions associated with the energy conversion take place at the two electrodes. During discharge (figure 3.1a), the negative electrode contains the substance that is oxidized (i.e. releases electrons), while the positive electrode contains the oxidizing substance that is reduced (i.e. accepts electrons). Those electrons pass through the external load, thereby doing useful work. When the battery is charged, this reaction is reversed and a corresponding amount of energy from an external source has to be supplied to the cell (figure 3.1b) [21].

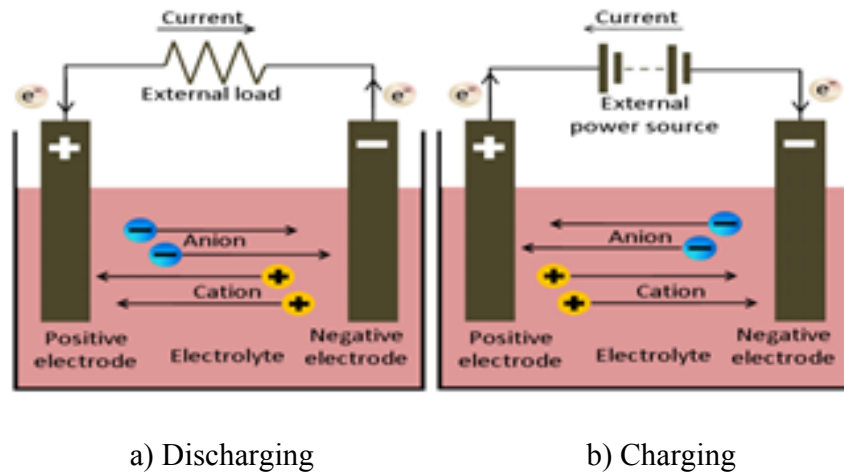


Fig. 3.1. Schematic representation of the operation of electrochemical cell

### 3.2.2 Current flow and polarization

The current in the battery arises from the transfer of electrons from one electrode to the other. When there is no current flow through a cell, the difference between the potentials of the positive and negative electrodes gives an open-circuit voltage (OCV) of the cell. When current flows, however, mass transport is required to bring the reacting substances to the electrode surface or carry them away. [12] As a result, the voltage under current flow is different from the OCV and the difference comprises (i) an overvoltage at the electrodes caused by electrochemical reactions and concentration deviations on account of transport phenomena and (ii) ohmic voltage drops caused by the electronic as well as the ionic current flows in the conducting parts including the electrolyte, current-collectors and active masses [21, 22]. The sum of both, called polarization, is responsible for a decreased cell voltage ( $V_{dis}$ ) during discharge and an increased cell voltage ( $V_{ch}$ ) during charge as shown below.

$$V_{dis} = E_0 - V_{op+} - V_{op-} - I \cdot R_{pol} \quad (3.1)$$

$$V_{ch} = E_0 + V_{op+} + V_{op-} + I \cdot R_{pol} \quad (3.2)$$

where  $V_{op+}$  and  $V_{op-}$  are the overvoltages at the positive and negative electrodes, respectively, and  $R_{pol}$  stands for the polarization resistance. Due to the polarization effects, the battery voltage under current flow may differ substantially from the OCV depending on the state-of-charge of the battery. These two polarization terms are important components for battery model development.

### 3.2.3 Other factors affecting battery models

Other important factors affecting battery performance and models include: battery capacity, state-of-charge (SOC), rate of charge and discharge, temperature, and age [22].

The battery capacity represents the maximum amount of energy that can be extracted from the battery under certain conditions, and is determined by the mass of active material contained in the battery.

The charging/discharging rates affect the rated battery capacity. According to the Peukert's equation, if the battery is being discharged very quickly, then the amount of energy that can be extracted from the battery is reduced [21, 22]. Consequently, effective modeling of Peukert's relation is particularly important for design and analysis of power converter controlled battery charge and discharge.

The age and history of a battery have impacts on the capacity of a battery. Even when following manufacturers' DOD (depth of discharge) specifications, the battery capacity only stays at the rated capacity for a limited number of charge/discharge cycles. If the battery has been taken below its maximum DOD during its usage, battery capacity may be prematurely reduced.

The temperature of a battery also affects the energy that can be extracted from the battery. At higher temperatures, the battery capacity is usually higher than that at lower temperatures. But, intentionally elevating battery temperature is not an effective method to increase battery capacity as this also decreases battery lifetime.

### 3.3. Mathematical Battery Models

A detailed mathematical battery model normally includes several sub-models. The most vital sub-model for electrical system study is the voltage-current model, which describes how the terminal voltage of a battery changes with the current. One of the best known voltage-current model for constant-current discharge is the Shepherd model [6, 8]:

$$V_{batt} = E_0 - K \left[ \frac{Q}{Q - it} \right] i - R_0 i \quad (3.3)$$

Many recent voltage-current models are more complicated than the Shepherd's relation [4, 7, 8]. Those models typically start with a relation similar to that of Shepherd, and then add and modify terms to try to 1) improve the fit of the relation to both measured charge and discharge curves, and 2) relax the assumptions behind the Shepherd model.

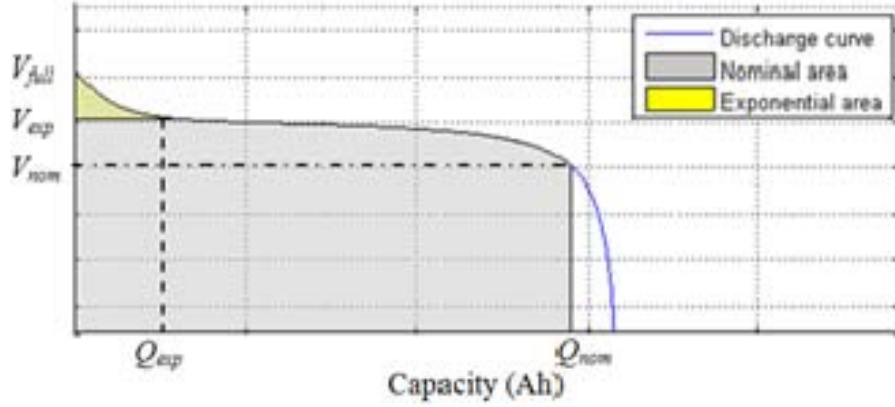


Fig. 3.2. Typical battery discharge curve

Equations (3.5) and (3.6) present modified battery models [5] for discharge and charge of lead-acid batteries, respectively, based on the Shepherd relation and SimPowerSystems battery model [22],

$$V_{dis} = E_0 - K_{dr} \frac{Q}{Q-it} i^* - R_0 i - K_{dv} \frac{Q}{Q-it} it + Exp(t) \quad (3.5)$$

$$V_{ch} = E_0 - K_{cr} \frac{Q}{it + \lambda \cdot Q} i^* - R_0 i - K_{cv} \frac{Q}{Q-it} it + Exp(t) \quad (3.6)$$

where  $K_{dr}$  is the polarization resistance coefficient ( $\Omega$ ) and  $K_{dv}$  is the polarization overvoltage coefficient ( $V/Ah$ ). In (3.5) and (3.6), the second term, regarding the polarization *ohmic* voltage drop, is different for charge and discharge and is modified by using a filtered battery current  $i^*$  to simulate actual slow voltage dynamic behavior for a step current response. The coefficient  $\lambda$  in (3.6) is to account for the shift of the polarization resistance during the charge of the battery [22]. The internal resistance in the third term has different values for charge and discharge. A fourth term concerning the polarization overvoltage is added. This term together with  $E_0$  can better

represent the nonlinear OCV relation with the *SOC*. The last term  $Exp(t)$  represents an exponential dynamic voltage (figure 3.2) to reflect a non-linear hysteresis phenomenon between discharge and charge [22]. For lead-acid batteries,  $Exp(t)$  is determined by (3.7), where  $u(t)=0$  for discharge and  $u(t)=1$  for charge. Equations (3.5) and (3.6) can be rewritten by using SOC. For example, in terms of SOC, (3.5) becomes (3.8), which shows that as *SOC* reduces, the voltage drop, caused by polarization ohmic and overvoltage impacts, increases under battery discharge mode. Also, according to (3.8), the polarization overvoltage impact is insignificant in the vicinity of the full battery capacity but becomes a more dominant component as the SOC drops.

$$\dot{Exp}(t) = B \cdot i \cdot (Exp(t) + A \cdot u(t)) \quad (3.7)$$

$$V_{dis} = E_0 - K_{dr} \frac{I}{SoC} i^* - R_0 i - K_{dv} \left( \frac{I}{SoC} - 1 \right) + Exp(t) \quad (3.8)$$

Primary limitations associated with (3.5) and (3.6) contain: the battery capacity “*Q*” does not change with the current amplitude; the temperature does not affect the model’s behavior; the aging of the battery is not considered; the self-discharge is not included. Those factors can be considered in a more complete mathematical battery model as shown by figure 3.3 [23], in which battery parameters change during the lifetime of the battery to provide an ageing profile and degradation of battery performance affected by many other factors (figure. 3.3) [4, 23].

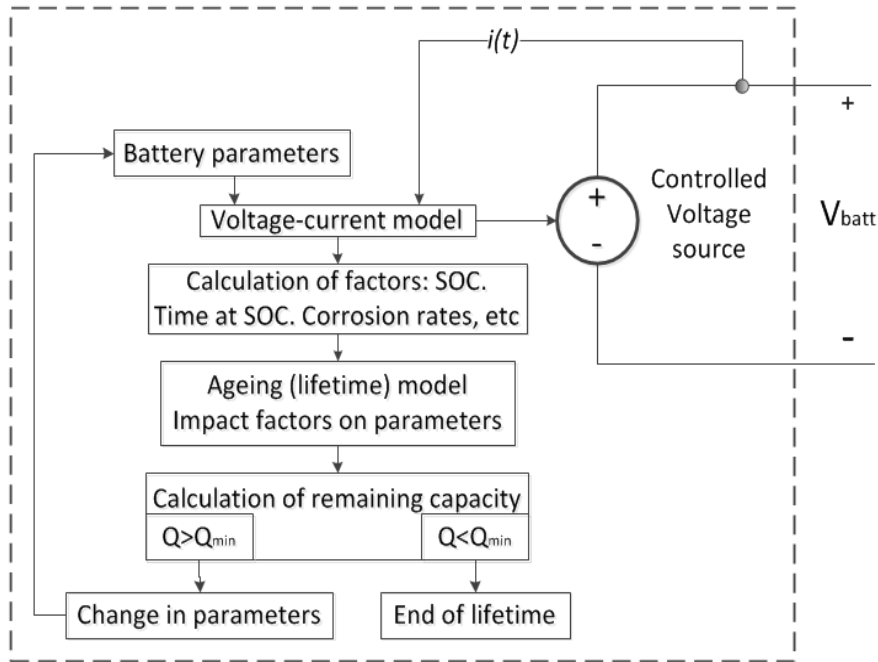


Fig. 3.3. Mathematical flow chart of a battery model [4]

The change in parameters is calculated at every simulation time step. For example, the *SOC* can be calculated more accurately at each time step based on (3.9), [23] which includes the impact of gassing current  $i_{gas}$  and the self-discharge current  $i_{sd}$ . If the capacity falls below the threshold capacity then the end of life of the battery is signaled.

$$SoC = SoC_{init} - \int_0^t (i - \max(i_{gas}, i_{sd})) \cdot d\tau / Q \quad (3.9)$$

### 3.4. Circuit-Oriented Battery Models

Circuit-oriented battery models use a combination of voltage and current sources, resistors, and capacitors to model battery performance. Most of these electrical models fall under three basic categories: Thevenin-based [10]–[16], impedance-based [17], [18], and runtime-based

models [9], [19]. Normally, it is more complicated to change battery parameters for different conditions and states of the battery.

In its most basic form, a Thevenin-based model [10]–[16], shown in figure 3.4(a), consists of a voltage source [at  $V_{oc}(SOC)$ ] in series with a resistor (internal resistance  $R_0$ ) and a parallel combination of a capacitor and resistor to predict battery response to transient load events at a particular  $SOC$ , by assuming the open-circuit voltage [ $V_{oc}(SOC)$ ] is constant. Thus, this model is unable to reflect the  $SOC$  influence to the battery behavior properly.

Impedance-based models, shown in Figure 3.4(b), employ the method of electrochemical impedance spectroscopy to obtain an ac-equivalent impedance model in the frequency domain, and then use a complicated equivalent network ( $Z_{ac}$ ) to fit the impedance spectra [9, 19, 24]. The fitting process is difficult and complex. In addition, impedance-based models only work for a fixed  $SOC$  and temperature setting [17], and therefore they cannot predict dc response or battery runtime.

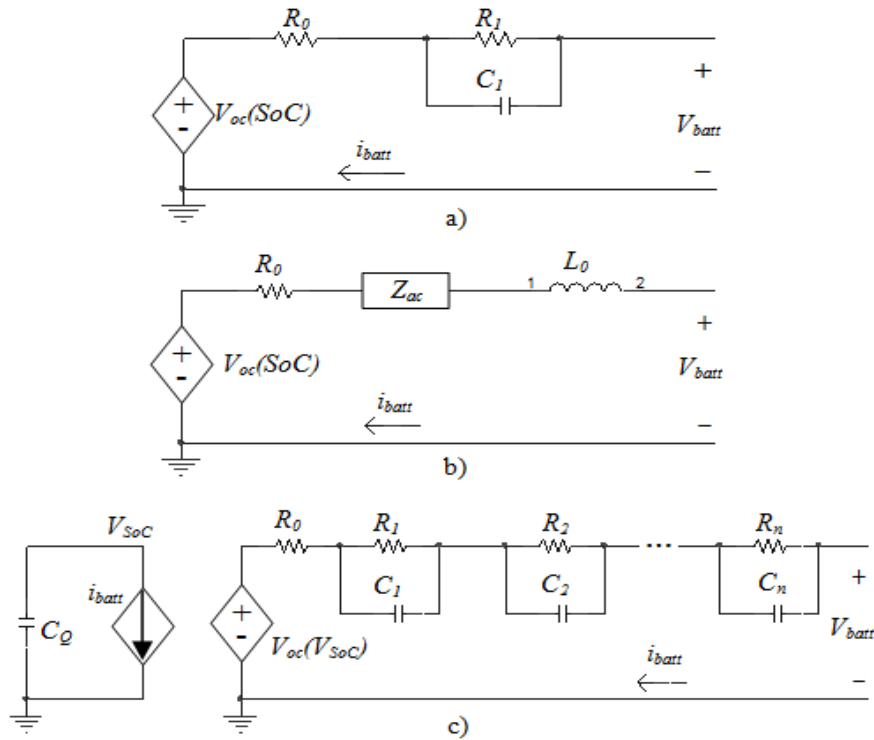


Fig. 3.4. Circuit-oriented battery models [9, 19]

Runtime-based models [9, 19] use a complex circuit network to simulate battery runtime and dc voltage response. Figure 3.4(c) shows a recent runtime-based battery model [19]. On the left side of the model, a capacitor ( $C_0$ ) having the value of battery capacity plus a current-controlled current source describes how the battery SOC, represented by  $V_{SoC}$ , varies with the battery current. On the right side, the RC networks, similar to that used in the Thevenin-based model, simulate the relation between the battery current and terminal voltage.

The relation between the mathematical and circuit-based battery models can be evaluated through a comparison study of battery discharge between figure 3.4c and (3.8) in the following ways.

a) The term of  $R_0 i_{batt}$  is equivalent to  $R_0 i_d$  in (3.7), which represents the internal resistance voltage loss in circuit-based and mathematical battery models, respectively.

b) For the RC networks of the runtime-based battery model, assuming that the voltage applied to the  $i_{th}$  RC network is  $v_i$ , then, in the Laplace transform domain, the relation between the voltage  $v_i$  and the battery current passing through the  $i_{th}$  RC network is (3.10). According to (3.10), the voltage  $v_i$  can be interpreted as the voltage drop of the low-pass filtered battery current over the resistor  $R_i$  of the RC network, in which the cut off frequency of the low-pass filter is  $1/(R_i C_i)$ . Thus, the combined effect of all the RC networks is actually equivalent to a resultant low-pass filter applied to a resultant RC network resistance. From this point of view, the low-pass filtered current in the circuit-based model is equivalent to  $i^*$  in (3.8), and the voltage drop over the RC networks together is equivalent to the term  $Kdr \cdot i^*/SOC$  in (3.8) to reflect the polarization ohmic voltage drop. But, the term  $Kdr \cdot i^*/SOC$  in the mathematical-based model is a function of SOC, which implies that the values of  $R_i$  and  $C_i$  of the RC networks in the circuit-based model should be also functions of SOC (consistent with results shown in [9], [19]).

$$v_i(s) = R_i \frac{1/(R_i C_i)}{s + 1/(R_i C_i)} i_{batt}(s) \quad (3.10)$$

c) In the runtime-based battery model, the battery OCV is modeled by a voltage-controlled voltage source, in which voltage  $V_{SOC}$  simulates the battery SOC. A comparison between the open-circuit voltage  $V_{oc}(V_{SOC})$  in the circuit-based battery model and (3.8) indicates that  $V_{oc}(V_{SOC})$

should be equivalent to  $E_{\theta} - K_{dv} \cdot (1/SOC - 1)$ . As a result,  $V_{oc}(V_{SoC})$  in the circuit-based model should be a function of  $SOC$  too (consistent with results shown in [9], [19]).

d) Different from figure 3.3, it is normally more complex to model electrochemical phenomenon associated with the charging or discharging regimes, the age and past history of the battery, and the temperature in the circuit-based battery model. But, those issues are very important for research of converter controlled management of batteries that are connected to the grid.

### **3.5. Parameter Extraction for Mathematical and Circuit-Oriented battery Models**

The parameter extraction is a necessary step for both mathematical and circuit-oriented battery models and the mechanisms used for the parameter extraction are different for the two modeling approaches. For mathematical battery model, the fundamental voltage-current relationship associated with the  $SOC$ , as shown by figure 3.2, is built into the model. For the circuit-oriented battery model, however, the impact of  $SOC$  to the circuit parameters is not directly available. Hence, to gain the relation of circuit parameters over  $SOC$ , more expensive computational power is required.

#### **3.5.1 Parameter extraction of mathematical battery model**

The parameter extraction of a mathematical battery model can be achieved based on the manufacturer's battery steady-state characteristics. One way for the parameter extraction is to

build a system of equations based on several critical points selected from the steady-state characteristics. Then, model parameters can be obtained by solving the system equations.

Another approach used in this chapter for a comparison study is to extract model parameters through the regression technique [16, 17]. The regression method partitions a measurement into a model estimation part plus a residual  $\varepsilon_i$  as

$$v_{batt}(i) = f(\mathbf{X}, \boldsymbol{\beta}) + \varepsilon_i \quad i=1, 2, \dots, N \quad (3.11)$$

where  $f(\bullet)$  is a pre-defined function,  $\mathbf{X}$  is predictor variable vector,  $N$  is the number of the measurements,  $v_{batt}(i)$  is the  $i$ th observation,  $\boldsymbol{\beta}$  is the battery parameter vector. The parameter extraction of a battery mathematical model is obtained by fitting the model to a set of more data points collected from the steady-state characteristics. Fitting refers to calculating values of the parameter  $\boldsymbol{\beta}$  so as to minimize sum of square as shown by (3.12) for a larger data set over a wide *SOC* range.

$$err(\boldsymbol{\beta}) = \sum_{i=1}^N (v_{batt}(i) - f(\mathbf{X}_i, \boldsymbol{\beta}))^2 \quad (3.12)$$

### 3.5.2 Parameter extraction of circuit-oriented battery model

The parameter extraction for the runtime-based circuit-oriented battery model is computational expensive. For each *SOC* value, circuit parameters must be estimated first, which is normally based on a strategy of minimizing the RMS error between measured and equivalent-circuit-estimated battery terminal voltages [9, 19]. Let  $v_{batt}$ , an  $m$  dimensional vector ( $m$  is the

sampling points), be the battery terminal voltage obtained from experiment under a *SOC* value, and  $v'_{batt}$  be the estimated battery terminal voltage obtained from the model. The modeling error is  $err = v_{batt} - v'_{batt}$ . During the parameter extraction process for each *SOC* value, the estimated battery voltage is considered as a function of battery circuit parameter vector  $\alpha = \{V_{oc}, R_0, R_1, C_1, \dots, R_n, C_n\}$ , i.e.,  $v'_{batt} = f(\alpha)$ . Then, using typical least square fitting approach solved by Gauss-Newton algorithm, the circuit parameters for a given *SOC* can be estimated in the following steps:

- 1) Initial parameter estimation:  $\alpha^0 = \{V_{oc}^0, R_0^0, R_1^0, C_1^0, \dots, R_n^0, C_n^0\}$
- 2) Mismatch calculation:  $err = v_{batt} - v'_{batt} = v_{batt} - f(\alpha^0)$
- 3) Compute Jacobain matrix:  $J = \frac{\partial err}{\partial \alpha}$
- 4) Compute correction  $\Delta\alpha$  and update parameters:  $\alpha^{k+1} = \alpha^k + \Delta\alpha$
- 5) Repeat steps (2) to (4) until a stop criterion is reached, such as  $|err| < \varepsilon$  ( $\varepsilon$  is a predefined threshold).

Then, the updated  $\alpha$  is taken as the optimal solution for measured battery voltages under a specified discharge mode at one *SOC* value. When the process of the parameter extraction is completed for all *SOC* values, a curve of each circuit parameter over *SOC* is obtained. To build a battery model using a circuit simulation tool, curve fitting by using the nonlinear regression technique is necessary to obtain a mapping function of the circuit parameter over *SOC*. For example, for TCL PL-383562 polymer Li-ion batteries, the battery OCV over *SOC* is (3.13), the

internal resistance  $R_0$  over  $SOC$  is (3.14), and  $C_1$  over  $SOC$  function is (3.15) when two RC networks are used in the runtime-based battery model [9]. In reality, however, the mapping functions can be affected by many factors, such as measured battery voltages, conditions to perform the measurements, charge/discharge regimes, age and history of the battery, temperature, and mathematical models used for the curve fitting. Those factors may influence the circuit-based battery models in the following aspects: i) increased computational complexity, ii) reduced flexibility, iii) reduced stability, and/or iv) reduced accuracy

$$V_{oc}(SoC) = -1.031 \cdot e^{-35 \cdot SoC} + 3.685 + 0.2156 \cdot SoC - 0.1178 \cdot SoC^2 + 0.3201 \cdot SoC^3 \quad (3.13)$$

$$R_0(SoC) = 0.1562 \cdot e^{-24.37 \cdot SoC} + 0.07446 \quad (3.14)$$

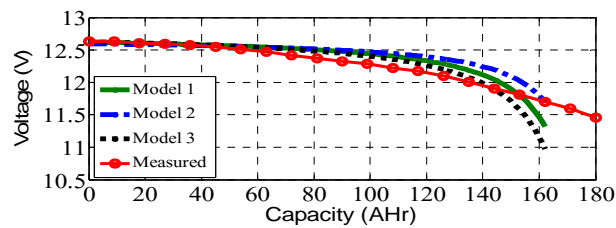
$$C_1(SoC) = -752.9 \cdot e^{-13.51 \cdot SoC} + 703.6 \quad (3.15)$$

### 3.6. Parameter extraction for mathematical and circuit-oriented battery models

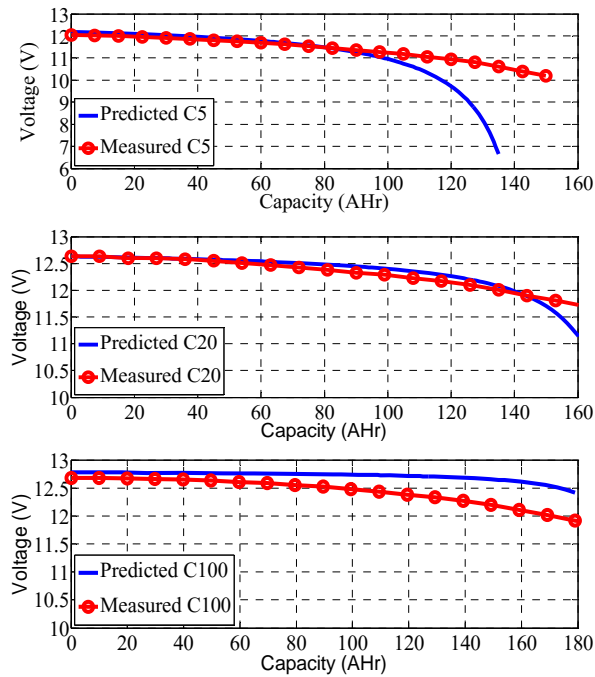
A comparison study is conducted for several mathematical battery models using different parameter extraction methods. In model comparison, both Shepherd and modified Shepherd models are analyzed. In parameter extraction, the investigation is focused on how different parameter extraction methods affect the performance of battery models. Charge and discharge characteristics are obtained for a 12V Trojan L-16 deep cycle lead-acid battery.

### 3.6.1 Shepherd discharge model under simple parameter extraction strategy

A simple parameter extraction strategy is to obtain battery model parameters by solving a system of equations. For the Shepherd model represented by (3.3), the parameters of  $E_0$ ,  $K$ , and  $R_0$  need to be identified, which requires to build a system of equations based on three points,  $[(Q_i, V_{batt_i}), i = 1, 2, 3]$ , selected from the discharge characteristics.



(a) Influence of data selection on model extraction



(b) Comparison between model prediction and measurement

Fig. 3.5. Performance of Shepherd model for a lead-acid battery

Then, a system of equations is obtained as shown by (3.16). But, an analysis of Equation (3.16) shows that a single unique solution of  $E_0$ ,  $K$ , and  $R_0$  cannot be obtained from (3.16). As a result, battery internal resistance  $R_0$  is normally specified. Then, to solve  $E_0$  and  $K$ , only two data points from the discharge characteristics are needed. Three discharge characteristic curves of the lead-acid battery relevant to C/100, C/20 and C/5 are used for the parameter extraction and performance study. The study shows that the performance of the Shepherd model depends strongly on which characteristic curve is used for the model extraction and what data points are selected.

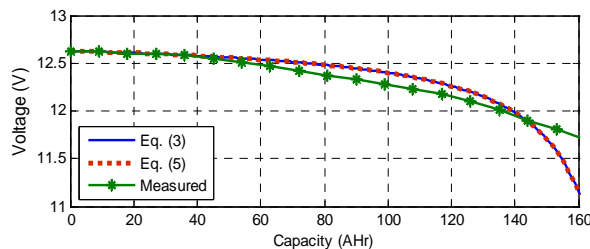
$$\begin{pmatrix} 1 & -Q \cdot i / (Q - Q_1) & -i \\ 1 & -Q \cdot i / (Q - Q_2) & -i \\ 1 & -Q \cdot i / (Q - Q_3) & -i \end{pmatrix} \begin{pmatrix} E_0 \\ K \\ R \end{pmatrix} = \begin{pmatrix} V_{batt\_1} \\ V_{batt\_2} \\ V_{batt\_3} \end{pmatrix} \quad (3.16)$$

Figure 3.5a shows three Shepherd battery models that are extracted based on three different groups of data selected from C/20 curve of the lead-acid battery. Each group of data contains two data points in order to solve parameters  $E_0$  and  $K$  associated with the Shepherd battery model. As it can be seen from figure 3.5(a), there is a slight difference in the estimated C/20 discharge characteristics among the three battery models that are extracted using different groups of data. It is also found that the model extracted based on C/20 characteristic curve may behave poorly under a different discharge rate of the battery as shown by figure 3.5(b), demonstrating a challenge for the Shepherd model that is both suitable for different battery types and for wide discharge conditions.

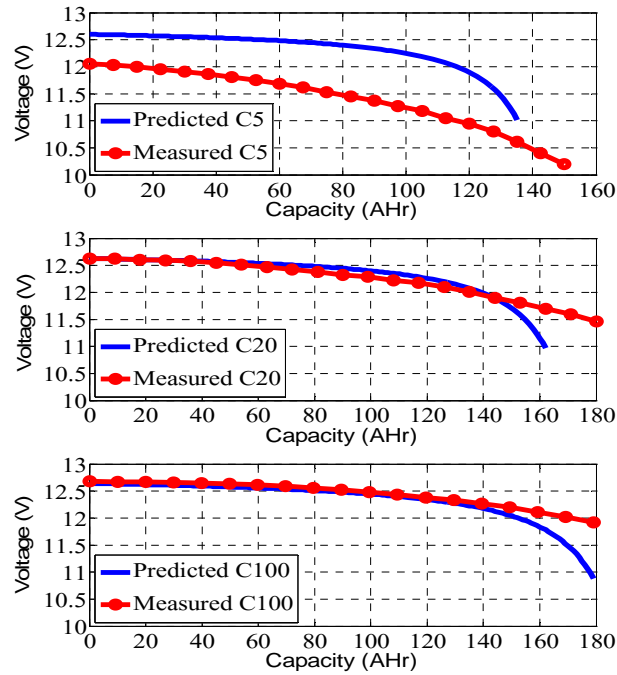
### 3.6.2 Modified shepherd model under simple parameter extraction strategy

For modified Shepherd discharge relation of the lead-acid battery represented by (3.5), the parameters of  $E_0$ ,  $K_{dr}$ ,  $K_{dv}$ ,  $R_0$  and  $A$  need to be identified, where  $A$  is a parameter associated with  $Exp(t)$  function [22]. Similar to the reason shown in Section 3.4, internal resistance  $R_0$  must be specified. Then, to solve  $E_0$ ,  $K_{dr}$ ,  $K_{dv}$  and  $A$ , a system of four equations is built based on four data points selected from the discharge characteristics as shown by (3.17). But, an examination of (3.17) shows that a single unique solution of  $E_0$ ,  $K_{dr}$ ,  $K_{dv}$  and  $A$  cannot be obtained from (3.17). In MatLab SimPowerSystems, it is assumed that  $K_{dr} = K_{dv}$ , which seems to agree with the analysis associated with equation (3.17) in this chapter. Under the assumption of  $K_{dr} = K_{dv}$ , the parameters of  $E_0$ ,  $K_{dr}$  and  $A$  can then be solved by building a system of three equations based on three data points selected from a discharge characteristic curve.

$$\begin{pmatrix} 1 & \frac{-Q \cdot i}{Q - Q_1} & \frac{-Q \cdot Q_1}{Q - Q_1} & Exp'(Q_1) \\ 1 & \frac{-Q \cdot i}{Q - Q_2} & \frac{-Q \cdot Q_2}{Q - Q_2} & Exp'(Q_2) \\ 1 & \frac{-Q \cdot i}{Q - Q_3} & \frac{-Q \cdot Q_3}{Q - Q_3} & Exp'(Q_3) \\ 1 & \frac{-Q \cdot i}{Q - Q_4} & \frac{-Q \cdot Q_4}{Q - Q_4} & Exp'(Q_4) \end{pmatrix} \begin{pmatrix} E_0 \\ K_{dr} \\ K_{dv} \\ A \end{pmatrix} = \begin{pmatrix} V_{batt\_1} + R_d i \\ V_{batt\_2} + R_d i \\ V_{batt\_3} + R_d i \\ V_{batt\_4} + R_d i \end{pmatrix} \quad (3.17)$$



(a) Comparison of Shepherd and modified Shepherd models



(b) Comparison between model prediction and measurement under different discharge rates

Fig. 3.6. Performance of modified Shepherd model for a lead-acid battery

Figure 3.6(a) shows a comparison between the Shepherd model and a modified Shepherd battery model that are extracted based on three data points selected from  $C/20$  curve of the lead-acid battery. Unlike the Shepherd model, one extra data point at the end of the exponential zone is added in order to solve parameters  $E_0$ ,  $K_{dr}$  and  $A$  associated with the modified Shepherd battery model (3.5). Then, the data selected from the  $C/20$  characteristic curve is used for model extraction of both models. Using the similar data points selected from the same  $C/20$  discharge characteristic curve, the extracted battery models based on (3.3) and (3.5) are very close as shown by figure. 3.6a. However, when the extracted battery model of (3.5) is used to evaluate battery performance under different discharge rates, large error may result as shown by figure 3.6b. This result is different from results shown in [5] and [6] for a NiMH battery, which implies

that the performance of the modified Shepherd battery model represented by (3.5) and (3.6) could vary largely from one battery type to another.

### 3.6.3 Parameter Extraction by Linear Regression

For comprehensive evaluation, linear regression approach is examined for parameter extraction of mathematical battery models. The regression approach requires the form of the function  $f$  in (3.11) to be predefined explicitly, making the regression approach more function dependent. Using the regression approach, it is possible to extract directly all the three parameters of  $E_0$ ,  $K$ , and  $R_0$  associated with Equation (3.3) or all the five parameters of  $E_0$ ,  $K_{dr}$ ,  $K_{dv}$ ,  $R_0$  and  $A$  associated with Equation (3.5). However, it is found that the parameter estimation through the direct regression extraction could deteriorate the performance of the model especially when the model is extracted under one discharge rate but is used for performance evaluation of different battery discharge rate. Similar to Sections 3.4-a and 3.4-b, it is found that specifying battery internal resistance  $R_0$  before applying the regression method is critical for both battery models of (3.3) and (3.5). In addition, for battery model of (3.5), it is important to assume  $K_{dr}=K_{dv}$  before using the regression method for parameter extraction. This seems to explain from another viewpoint the advantage of assuming  $K_{dr}=K_{dv}$  in SimPowerSystems.

Then, using the linear regression method for the battery model represented by (3.3), the predictor variable vector associated with the  $n_{th}$  observation is  $\mathbf{X}=(1, -i/SOC_n)$ , and the parameter vector is  $\boldsymbol{\beta}=(E_0, K)$ . For the battery model represented by (3.5), the predictor variable vector

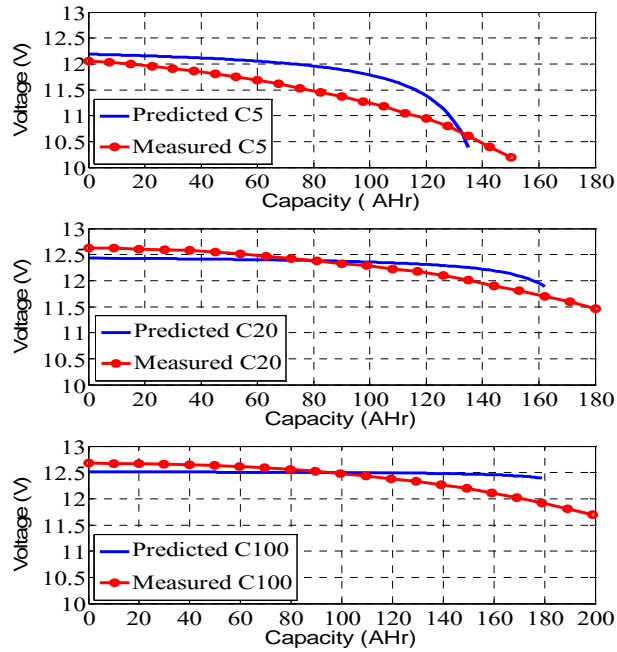
associated with the  $n$ th observation is  $\mathbf{X}_n=(1, 1-2/SoC_n, Exp'(Qn))$ , and the parameter vector is  $\boldsymbol{\beta}=(E_0, K_{dr}, A)$ .

Figure 3.7(a) shows the Shepherd model obtained by using the linear regression method based on the C/20 discharge characteristic curve of the lead-acid battery. Compared to figure 3.5, the performance does not improved significantly although more data points are utilized for the parameter extraction. This is due to the reason that the regression method depends strongly on the pre-defined function  $f(\bullet)$ . Therefore, if the function selected is not perfectly suitable to a battery type, the model performance could be affected considerably. Figure 3.7(b) shows the modified Shepherd model obtained by using the regression method based on C/20 discharge characteristics of the battery too. As it can be seen from figure 3.7(b), the extracted battery model tries to minimize the error between model estimated and measured battery output voltages under the C/20 discharge rate of the battery. However, when the extracted battery model is used for estimation under different discharge rates, large errors between prediction and measurement could result (figure 3.7(b)), demonstrating again the limitation of the regression method for parameter extraction of the battery models.

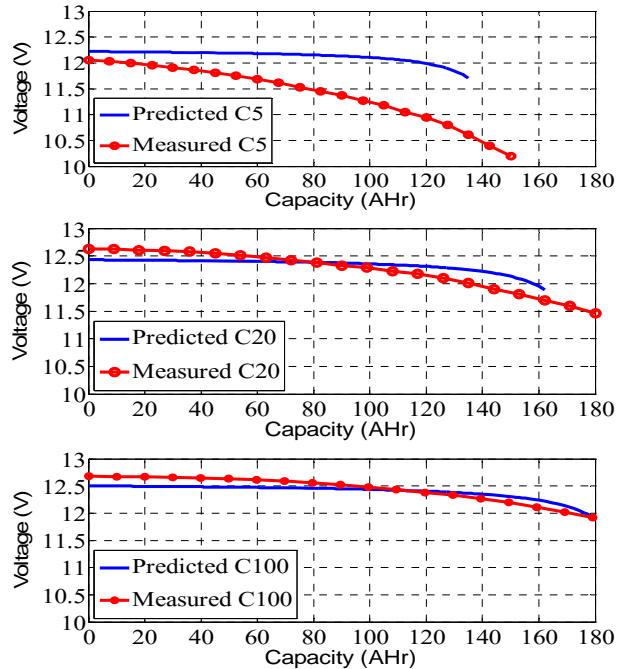
#### **3.6.4 Modified Shepherd Charge Model**

During the charge process of a battery, equation (3.6) should be used, which requires that parameters associated with (3.6) need to be identified first. Conventionally, two approaches have been used to identify parameters of the charge model. The first approach uses the same

parameters of the discharge model (3.5) [22]. The second approach uses different parameters that are extracted separately based on battery charge model and characteristics [23].



(a) Shepherd model



(b) Modified Shepherd model

Fig. 3.7. Comparison between model prediction and measurement for a lead-acid battery using linear regression method

Figure 3.8 shows a comparison of the predicted and measured charge characteristics, in which the charge model (3.6) uses the same parameters as those of the discharge model (3.5) used in figure 3.6. The charge rates are  $C/20$  and  $C/5$  in figure 3.8. The analysis shows that errors between predicted and measured charge characteristics exist, which is primarily affected by the effectiveness of discharge parameters applied to the charge model, the effectiveness of the modified Shepherd models applied to different battery types, and the difference of the exponential zones between the charge and discharge characteristics. The analysis shows that depending on the battery types, the parameters for charge and discharge models may need to be different.

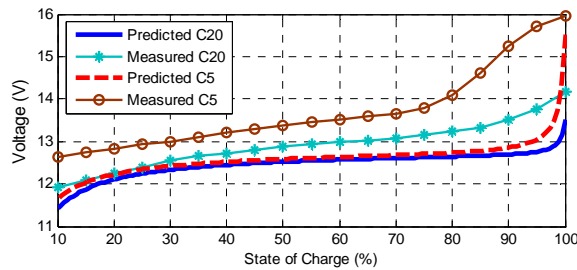


Fig. 3.8. Comparison between model prediction and measurement when the parameters used for charge and discharge models are the same

### 3.7. Conclusions

This chapter presents a comparison study of mathematical and circuit-oriented battery models with a focus on lead-acid batteries. For mathematical battery model, the fundamental voltage-current relationship associated with  $SOC$  is normally built into the model based on the Shepherd relation. For the circuit-oriented battery model, however, the impact of  $SOC$  to the circuit parameters is not directly available. Although the two modeling approaches are different,

there are certain relations between mathematical and circuit-oriented battery models. For example, the effect of the RC networks in modern runtime-based battery model is equivalent to the polarization resistance voltage impact in the mathematical battery model and the current-control voltage source in the circuit-oriented battery model is equivalent to the battery OCV minus polarization overvoltage effect in the mathematical battery model.

Regarding model extraction, parameters of a mathematical battery model can be obtained by either solving a system of equations or utilizing regression technique. But, the parameter extraction of runtime-based circuit-oriented battery models requires more expensive computational power. For the mathematical battery models, the performance of Shepherd and modified Shepherd models may vary for different battery types and also depends on what algorithms are used for the model extraction and how data are selected from the measured characteristic curves. Performance study demonstrates that the regression extraction strategy is affected strongly by the predefined function for a mathematical battery model. If a predefined function is not well suitable to a battery type, the extracted battery models using the regression technique may have a badly deteriorated performance.

## **CHAPTER 4**

### **GRID-SIDE CHARGER CIRCUIT CONFIGURATION OF EDVs CHARGING STATION**

#### **4.1 Topology of EDVs charging infrastructure in grid side system.**

As a high power charging infrastructure with desired functions, some particular structure and hardware are required. First, to provide a reliable and stable fast charging environment to a series of high capacity batteries, the rated power of the charging infrastructure has to satisfy the requirement of the EDVs. For example, the proposed charging station should be able to provide enough power when the station is fully loaded by EDVs. Second, the voltage of the DC bus has to possess a good stability. This factor is very important for EDVs, because the fastidious requirements of charging voltage and current are demanded by the EDVs batteries. Third, since the charging infrastructure has to realize both V2G and G2V processes, it is necessary to be able to control the power flow in both directions between grid side and EDVs side by a bi-directional AC/DC converter. Moreover, other factors, including the efficiency in power transition, quick response speed in an accurate way and stability in some extreme cases, are also crucial for the performance of the EDVs charging station when the overall cost should be as low as possible.

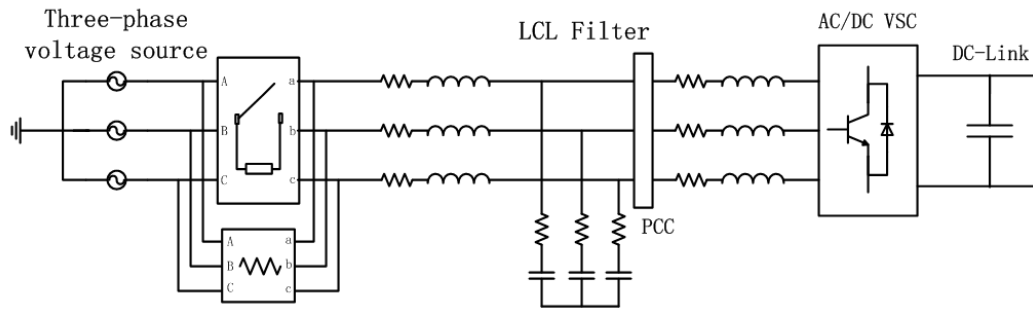


Fig. 4.1 Configuration of grid side system for EVs charging infrastructure

According to the factors above, the expected structure of the grid side converter system is shown in figure 4.1. In this system, the DC-Link capacitor who works as a DC bus is located on the right-hand side of the figure, while a three-phase voltage source is on the left-hand side of the circuit. The three-phase voltage source is introduced to represent the power grid and supply three-phase power to the charging infrastructure. In the middle of the grid-side system, a switching and a LCL grid filter are equipped to minimize the overshoot and high frequency oscillation. A further explanation will be presented about the hardware and control structure of the grid side system in the rest of this chapter.

## 4.2 Grid-side Converter (GSC)

Various AC/DC converters have been used for charging purpose with respect to different kinds of batteries in distinct application. For the EDVs charging station in the thesis, a three-phase conventional Voltage Source Converters (VSCs) controlled by Pulse Width Modulation (PWM) generating signal is used to achieve the expected performance. The PWM has been commonly used for the power control strategy. The main advantage of the PWM is a very low power loss for the switching devices. Especially, in the digital control mission, it is easy to set needed duty cycle by PWM. Since EDVs charging infrastructure has to cope with certain kinds

of functions, the flexibility of the duty cycle and power efficiency of PWM is important for the performance of the design in this thesis.

Regarding the AC/DC GSC, several kinds of semiconductor switches are employed at present, such as Power MOS Field Effect Transistors (Power MOSFETs), Gate Turn-Off Thyristors (GTOs), and Insulated Gate Bipolar Transistors (IGBTs). The IGBT combines the advantages of the MOSFETs and the advantages of the bipolar transistors by using an isolated gate FET as the control unit, and utilizing a bipolar power transistor as the switch to transmit high currents. The IGBT is usually used in medium to high power applications. The control unit in an IGBT is much simpler than a GTO, and the switch frequency can be up to 40 kHz. High power IGBT modules may consist of many devices in parallel and can have very high current handling capabilities [30]. The grid side AC/DC converter employs 6 IGBTs as shown in figure 4.2. As a grid-side bipolar voltage source converter, the GSC is able to satisfy several functions of EDVs charging infrastructure, such as converting AC power input to DC power output in the charging process and inverting the DC power input back into the AC power output when V2G process is proceeding. This converter plays an important role in transferring the power between grid side and the EDVs side of the integrated charging station. Therefore, it is critical to design the control scheme of the GSC carefully and make the GSC working efficiently.

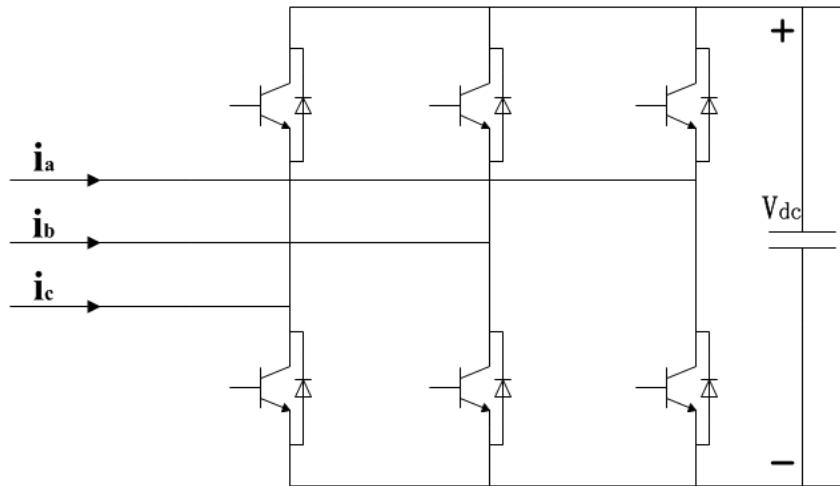


Fig. 4.2 A conventional AC/DC converter

### 4.3 LCL Filter design

In designed grid side AC/DC converter, it is extremely important to consider the influence of high frequency harmonics caused by conventional power devices that work under high switching frequency. Hence, a filter is equipped for the purpose of reducing the high frequency harmonics and preventing the other sensitive electric devices from disturbance and power losses. Considering the high frequency that the designed system working on, it is unfeasible to employ a high value inductance working as a high frequency filter, since it would enlarge the cost of system while the system dynamic response would become lower [31]. For this reason, a LCL filter is used for restricting high frequency current harmonics. Generally, three advantages could be achieved by the utilization of a LCL filter [32]. First, higher attenuation could be achieved at high frequencies since the LCL-filter increases the attenuation with 60dB/decade compared to the 20 dB/decade for the L-filter. Second, the total inductance of the LCL-filter is smaller than for the L-filter, this can reduce the physical size of the filter and simplifies the design and manufacture of the inductors. Third, since the total reactance of the LCL-filter is less than the L-

filter at low frequencies, the DC-link capacitor voltage drop caused by the LCL-filter is smaller than the L-filter in the same current and frequency.

For reducing high-order harmonics in the grid side system of the EDVs charging system, it is important to select appropriate parameters of the LCL filter; otherwise, not only a lower attenuation would happen, but also the oscillation effects may increase distortion in circuit. According to reference [31], the procedure about how to choose the parameters of LCL filter in grid side system is explained below.

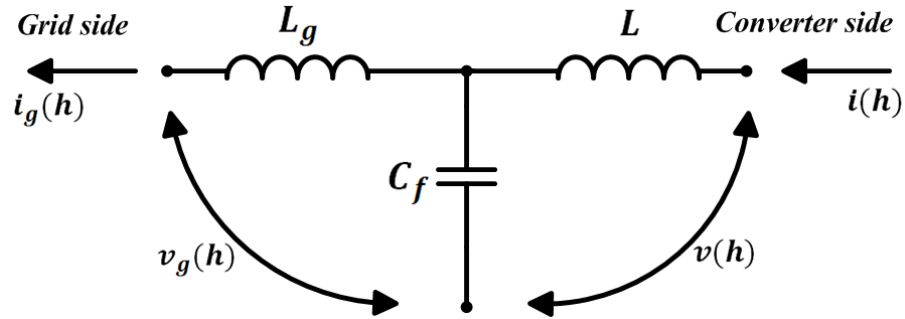


Fig. 4.3 Equivalent single-phase LCL filter at the  $h$  harmonic

First, to express the filter parameter in normalization, the base values of inductance and capacitance is given in equations (4.1), (4.2), in which  $E_n$  is line-to-line voltage,  $\omega_n$  is the grid frequency and  $P_n$  is the active power absorbed by the converter in rated conditions.

$$Z_b = \frac{(E_n)^2}{P_n} \quad (4.1)$$

$$C_b = \frac{1}{\omega_n Z_b} \quad (4.2)$$

Meanwhile, the resonance frequency is expressed by the switching frequency  $\omega_{sw}$  as shown in equation (4.3).

$$\omega_{res} = k \omega_{sw} \quad (4.3)$$

Neglecting all the resistors, an equivalent single-phase LCL filter configuration for the  $h$  harmonic is obtained as shown in figure 4.3, in which  $i(h)$  and  $v(h)$  indicate the harmonics of current and voltage, while  $h_{sw}$  is the order of the switching frequency harmonic. The current ripple attenuation is computed by considering the converter as a harmonic generator at high frequency when the grid is being seen as a short circuit. Therefore, the converter voltage harmonic is  $v(h_{sw}) \neq 0$  and the grid voltage harmonic is  $v_g(h_{sw}) = 0$  at the switching frequency. Then the ripple attenuation, passing from the converter side to the grid side, can be calculated with the following steps:

$$\frac{i_g(h_{sw})}{v(h_{sw})} = \frac{Z_{LC}^2}{\omega_{sw}L \cdot |\omega_{res}^2 - \omega_{sw}^2|} \quad (4.4)$$

$$\frac{i(h_{sw})}{v(h_{sw})} \approx \frac{1}{\omega_{sw}L} \quad (4.5)$$

$$\frac{i_g(h_{sw})}{i(h_{sw})} \approx \frac{Z_{LC}^2}{|\omega_{res}^2 - \omega_{sw}^2|} \quad (4.6)$$

where  $Z_{LC}^2 = [L_g C_f]^{-1}$ ,  $\omega_{res}^2 = (L_g + L)Z_{LC}^2/L$ ,  $\omega_{sw}^2 = (2\pi f_{sw})^2$ , ( $f_{sw}$  is the switching frequency), and  $h_{sw} = \omega_{sw}/\omega_n$  is the switching frequency harmonic order.

On the other hand, in order to make the filter properly damped, a resistor  $R_d$  is connected with the filter capacitor  $C_f$  in series. Then, the current-controlled system can be represented as equation (4.7).

$$G(s) = \frac{i(s)}{v(s)} = \frac{1}{Ls} \frac{(s^2 + R_d C_f Z_{LC}^2 s + Z_{LC}^2)}{(s^2 + R_d C_f \omega_{res}^2 s + \omega_{res}^2)} \quad (4.7)$$

And the power losses caused by the resistor  $R_d$  can be calculated by equation (4.8)

$$P_d = 3R_d \cdot \sum_h [i(h) - i_g(h)]^2 \quad (4.8)$$

The main terms of the sum in equation (4.8) are for the index  $h$  near the order of switching frequency harmonic  $h_{sw}$  and its multiples, since the damping actually prevent resonance happening by absorbing a certain range of the switching frequency ripple.

Next, several more limitations are necessary for parameter calculation.

- a) According to [33], the capacitor value is limited for neglecting overmuch decrease of the power factor at rated power.
- b) For the purpose of limiting the voltage drop in the grid side system, the inductance is assumed to no more than  $0.1pu$ . Otherwise, a higher dc-link voltage will be required to guarantee current controllability, which will result in higher switching losses [33].
- c) The resonant frequency should be in a range between ten times the line frequency and one-half of the switching frequency, to avoid resonance problems in the lower and upper parts of the harmonic spectrum.
- d) Passive damping must be sufficient to avoid oscillation, but losses cannot be so high to reduce efficiency [34].

Finally, the parameters can be designed in following steps with the equations and limitations worked out above.

- 1) Select the required current ripple on the converter side  $\rightarrow$  design the inductor  $L$ . The outer inductor value can then be determined as a function of  $L$ , using the index for the relation between the two inductances

$$L_g = rL \quad (4.9)$$

- 2) Select the reactive power absorbed at rated conditions  $\rightarrow$  determine the capacitor value. Take  $\alpha$  as a percentage of the reactive power absorbed under rated conditions. The capacitor value is limited by condition a) above.

$$C_f = xC_b \quad (4.10)$$

- 3) Select the desired current ripple reduction  $\rightarrow$  knowledge of  $r$  and then design the outer inductor  $L_g$ . The ripple attenuation, calculated neglecting losses and damping of the filter, is defined by (4.6) and can be rewritten, considering (4.9) and (4.10), as

$$\frac{i_g(h_{sw})}{i(h_{sw})} = \frac{1}{|1 + r(1 - a \cdot x)|} \quad (4.11)$$

In equation (4.11),  $a = LC_b \omega_{sw}^2$  is a constant. Before using (4.11) to calculate  $r$ , the desired attenuation should be multiplied by a factor that takes into account the losses and the damping. If the sum of the two inductances does not respect condition (b), another attenuation level should be chosen, or another value for the absorbed reactive power should be selected as per step 2).

- 4) Verify the resonant frequency obtained

$$\omega_{res} = \sqrt{\frac{L_g + L}{LL_g C_f}} \quad (4.12)$$

Which can be written, referring to (4.3), (4.9), and (4.10), as

$$k = b \cdot \sqrt{\frac{1+r}{rx}} \quad (4.13)$$

Where  $b = 1/\omega_{sw} \sqrt{C_b L_g}$  is a constant. The resonant frequency is limited by condition (c). If this is not correct, the absorbed reactive power returned in step 2) or the attenuation returned in step 3) should be changed.

- 5) Set the damping according to condition d) above. At the resonant frequency the impedance of the filter is zero. The aim of the damping is to insert an impedance at this frequency to avoid oscillation. Hence, the damping value is set to a similar order of magnitude as the series capacitor impedance at the resonant frequency [35].

If the filter attenuation is not adequate, the design procedure returns to step 3) to increase the multiplication coefficient that takes into account the decrease of the filtering action due to losses. If this is not sufficient, the design procedure should go back to step 2) and select a higher value of the reactive power.

- 6) Verify the filter attenuation under other load conditions and with other switching frequencies, which has been explained in [31].

#### **4.4 Pre-charging strategy**

Concerning the capacitors in the circuit of the EDVs charging infrastructure, a pre-charging procedure plays an important role for preventing the components of the circuit from the damage caused by current overshooting. Figure 4.4 shows the current ripple at the beginning of the charging process, when the capacitors in the circuit do not be pre-charged. In figure 4.4, a severe current ripple happens at the beginning of the process. Even though the duration of the current ripple is no longer than 0.1 seconds, some sensitive circuit components may still be damaged. Hence, a pre-charging process is employed in this thesis in order to avoid the current ripple. Because the expected voltage of DC-Link capacitor is 700V, the voltage of the DC-Link capacitor should be no less than 500V after the pre-charging process. Moreover, the capacitors at the EDVs side filters also require pre-charging process to avoid intrusive current caused by the potential difference between the battery and the filter capacitor at the beginning of the charging process.

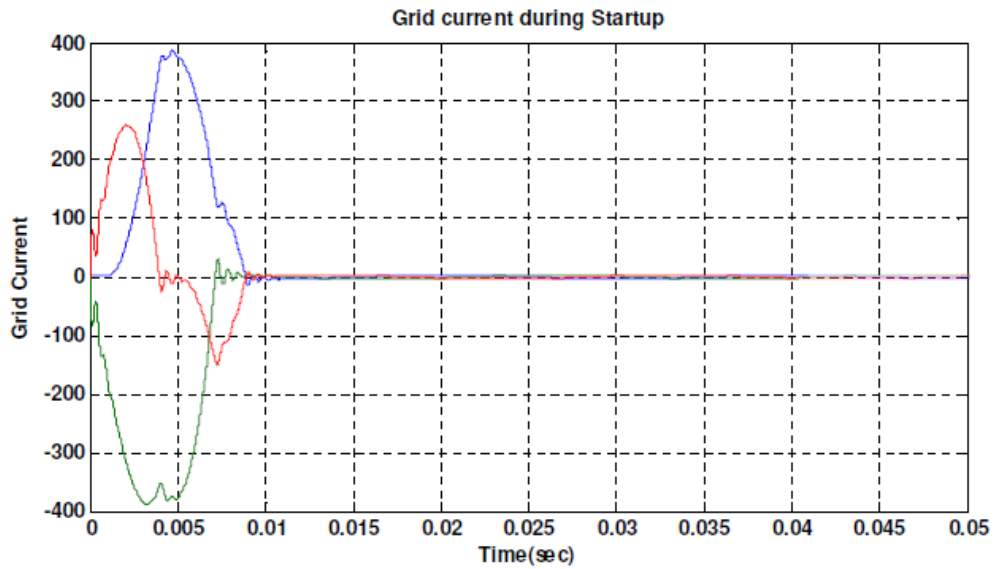


Fig 4.4 Current ripple at the beginning of the charging process

For the purpose of realizing pre-charging process, it is feasible to pre-charge the DC-Link capacitor to peak line-to-line voltage through the GSC. As shown in the figure 4.1, a series of resistors parallel connect with the switch in the grid side circuit. During the pre-charging process, the charging current is extracted from the grid to the DC-Link capacitor through the parallel resistors and the GSC. Although there is a current leap at the beginning of pre-charging caused by the low voltage of the capacitor, it could be limited under an acceptable value when an applicable resistance for the resistors is selected. Meanwhile, the GSC works as a diode rectifier at this moment since the controller of the integrated EDVs charging station is not active. The DC-Link capacitor can be charged to peak of line to line voltage in a very short time, while the capacitor of the EDVs side filter is also being charged. Once the pre-charging process is completed, the switch will be closed and the resistors become a by-pass of the switch. Since the pre-charging procedure sustains a very short time, the loss caused by the resistors would be very low.

#### 4.5 Vector control in $d$ - $q$ reference frame theory

Due to drawbacks [36] of the conventional vector control strategy, a direct-current vector control strategy is employed in the thesis [37]. The purpose of this session is to depict vector control scheme.

##### 4.5.1 Space vectors definition

In order to make the current vector control available, it is necessary to transform the three-phase stationary coordinate system into a two-phase rotating coordinate system. According to the reference [38], the procedure of transmission is described below..

First, the three phases instantaneous current  $i_a$ ,  $i_b$ ,  $i_c$  can be represented in the complex stator current vector  $\bar{i}_s$  as shown in (4.14).

$$\bar{i}_s = i_a + \alpha i_b + \alpha^2 i_c \quad (4.14)$$

In the equation (4.14) the spatial operators  $\alpha = e^{j\frac{2}{3}\pi}$  and  $\alpha^2 = e^{j\frac{4}{3}\pi}$ . The stator current complex space vector is shown in figure 4.5.

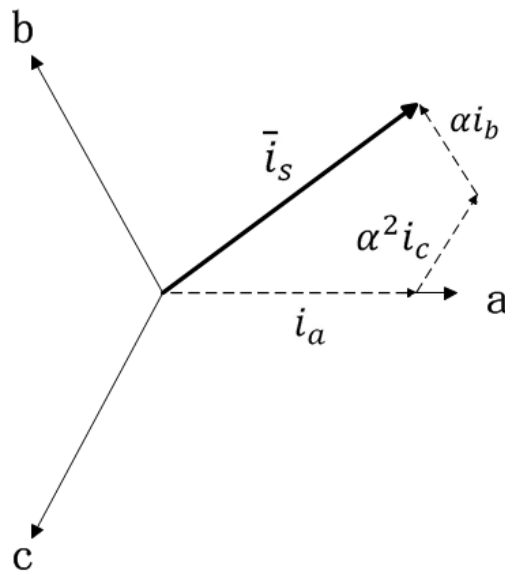


Fig. 4.5 Complex stator current vector  $\bar{i}_s$  and the component in  $(a, b, c)$

Then, two transformations are employed to transform between three-phase stationary coordinate system into a two-phase rotating coordinate system.

- a) Clarke transformation ( $abc$  system to  $\alpha\beta$  system).
- b) Park transformation ( $\alpha\beta$  system to  $dq$  system).

By Clarke transformation, the three phase current ( $a,b,c$ ) is expressed by another reference frame with only two orthogonal axis called ( $\alpha,\beta$ ). Then, we can get the following vector diagram. The axis- $\alpha$  and the axis- $a$  are assumed in the same direction.

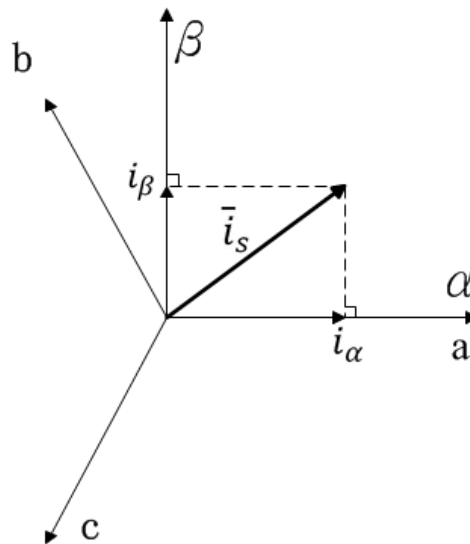


Fig 4.6 Clarke transformation

Through the Clarkson transformation (figure 4.6), the three-phase current is projected to axis  $\alpha$  and axis  $\beta$ , which is shown in the equation below.

$$\begin{cases} i_\alpha = i_a \\ i_\beta = \frac{1}{\sqrt{3}}i_a + \frac{2}{\sqrt{3}}i_b \end{cases} \quad (4.15)$$

Next, the two-phase orthogonal system, which is obtained by Clarkson transformation, is further converted into  $d, q$  rotating reference frame by Park Transformation. Assuming axis  $d$  is

aligned with grid voltage position; the result is shown in the figure 4.7 and equation (4.16) below, where  $\theta = \omega t$  represents the grid voltage rotating position.

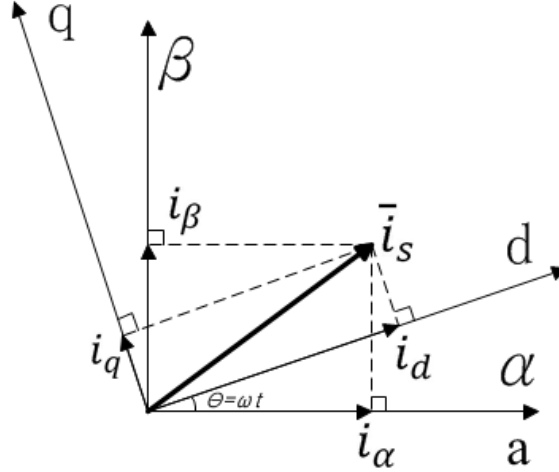


Fig 4.7:  $d, q$  rotating reference frame obtained by Park Transformation

$$\begin{cases} i_d = i_\alpha \cos \theta + i_\beta \sin \theta \\ i_q = -i_\alpha \sin \theta + i_\beta \cos \theta \end{cases} \quad (4.16)$$

Finally, the transformation between three-phase  $a, b, c$  system and  $d, q$  rotating reference frame in current can be shown as a matrix form below [37].

$$\begin{bmatrix} i_d \\ i_q \end{bmatrix} = \sqrt{\frac{2}{3}} \begin{bmatrix} \cos(\omega t) & \cos(\omega t - \frac{2}{3}\pi) & \cos(\omega t + \frac{2}{3}\pi) \\ -\sin(\omega t) & -\sin(\omega t - \frac{2}{3}\pi) & -\sin(\omega t + \frac{2}{3}\pi) \end{bmatrix} \begin{bmatrix} i_a \\ i_b \\ i_c \end{bmatrix} \quad (4.17)$$

The voltage between three-phase  $a, b, c$  and  $d, q$  rotating reference frame has the same relation.

$$\begin{bmatrix} v_d \\ v_q \end{bmatrix} = \sqrt{\frac{2}{3}} \begin{bmatrix} \cos(\omega t) & \cos(\omega t - \frac{2}{3}\pi) & \cos(\omega t + \frac{2}{3}\pi) \\ -\sin(\omega t) & -\sin(\omega t - \frac{2}{3}\pi) & -\sin(\omega t + \frac{2}{3}\pi) \end{bmatrix} \begin{bmatrix} v_a \\ v_b \\ v_c \end{bmatrix} \quad (4.18)$$

#### 4.5.2 Grid-side converter system schematic

In terms of the LCL filter located between three-phase voltage source and GSC, the Point of Common Coupling (PCC) is set between branch  $C$  and  $L_f$  of the LCL filter as shown in figure 4.1. Then, the grid-side converter schematic can be seen as figure 4.8, in which the left-hand part circuit of the PCC in the figure 4.1 is replaced by a three-phase voltage source and the grid side AC/DC converter is connected with the three-phase voltage source by a pair of resistor and inductor.

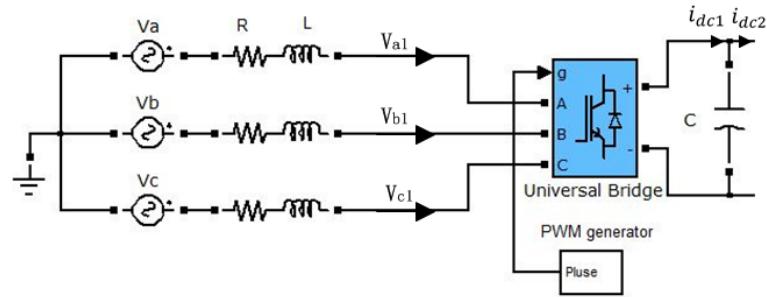


Fig 4.8 Grid-side converter system

It is easy to get the relationship between voltage at the PCC and output of the GSC [37] as shown in equation (4.19):

$$\begin{bmatrix} v_a \\ v_b \\ v_c \end{bmatrix} = R_f \begin{bmatrix} i_a \\ i_b \\ i_c \end{bmatrix} + L_f \frac{d}{dt} \begin{bmatrix} i_a \\ i_b \\ i_c \end{bmatrix} + \begin{bmatrix} v_{a1} \\ v_{b1} \\ v_{c1} \end{bmatrix} \quad (4.19)$$

To transform equation (4.19) into  $d$ - $q$  reference frame, equation (4.20) is derived by defining angular velocity as  $\omega_s$  and the matrix (4.18).

$$\begin{bmatrix} v_d \\ v_q \end{bmatrix} = R \begin{bmatrix} i_d \\ i_q \end{bmatrix} + L \frac{d}{dt} \begin{bmatrix} i_d \\ i_q \end{bmatrix} + \omega_s L \begin{bmatrix} -i_q \\ i_d \end{bmatrix} + \begin{bmatrix} v_{d1} \\ v_{q1} \end{bmatrix} \quad (4.20)$$

When axis- $d$  stands for real part and axis- $q$  represents imaginary part in the space vector theory, equation (4.20) also can be written as equation (4.21) and (4.22) in steady-state condition.

$\vec{V}_{dq}$ ,  $\vec{V}_{dq1}$  and  $\vec{I}_{dq}$  respectively represent the PCC voltages, grid side converter output voltage and grid current under steady-state condition.

$$\vec{v}_{dq} = R \cdot \vec{i}_{dq} + L_f \frac{d\vec{i}_{dq}}{dt} + j\omega_s L_s \cdot \vec{i}_{dq} + \vec{v}_{dq1} \quad (4.21)$$

$$\vec{V}_{dq} = R \cdot \vec{I}_{dq} + j\omega_s L_s \cdot \vec{I}_{dq} + \vec{V}_{dq1} \quad (4.22)$$

#### 4.5.3 Real power and reactive power of the grid side system

Regarding to the PCC voltage orientation frame, the axis- $d$  of the rotating reference frame is aligned with the grid voltage position. As a result, the three-phase voltage at the PCC projecting to the axis- $d$  reference frame would keep constant, while the corresponding  $q$ -axis voltage is zero. Then, the instantaneous real power and reactive power generated by the three-phase voltage source and absorbed by the GSC can be obtained by equation (4.23) and (4.24).

$$p = \text{Re}(\vec{v}_{dq} \vec{i}_{dq}^*) = v_d i_d + v_q v_q = v_d i_d \quad (4.23)$$

$$q = \text{Im}(\vec{v}_{dq} \vec{i}_{dq}^*) = v_q i_d - v_d i_q = -v_d v_q \quad (4.24)$$

Since the voltage in  $d$ -axis reference frame is equal to a constant and  $q$ -axis is zero as mentioned before, the current from the grid to the GSC under steady-state condition can be calculated by transforming equation (4.22) to equation (4.25), in which resistor  $R$  is neglected and  $\vec{v}_{dq1} = v_{d1} + jv_{q1}$ .

$$\vec{I}_{dq} = \frac{\vec{V}_{dq} - \vec{V}_{dq1}}{j\omega_s L} = \frac{\vec{V}_{d1} - \vec{V}_d}{j\omega_s L} - \frac{\vec{V}_{q1}}{\omega_s L} \quad (4.25)$$

As a result, the real power and reactive power absorbed by the GSC can be calculated by solving equations achieved above, as shown in equations (4.26) and (4.27). Referring to equation

(4.26) and (4.27), the real power and reactive power can be generally controlled by  $\vec{v}_{q1}$  and  $\vec{v}_{d1}$ , respectively. Since the resistance of R is a very small value compared with other elements in the equation, the relationship between power ( $P_{ac}, Q_{ac}$ ) and voltages ( $\vec{v}_{q1}, \vec{v}_{d1}$ ) are still established when the resistor R is neglected.

$$P_{ac} = -\frac{\vec{V}_d \vec{V}_{q1}}{j\omega_s L} \quad (4.26)$$

$$Q_{ac} = \frac{\vec{V}_d}{j\omega_s L} (\vec{V}_d - \vec{V}_{d1}) \quad (4.27)$$

## 4.6 Purposed current loop control strategy

### 4.6.1 Inner current control loop

The inner current loop strategy is based on the equations (4.28) and (4.29), which represents the relationship between the GSC output voltage and the voltage and current of PCC in  $d, q$  reference frame. The equations (4.28), (4.29) are derived by reducing the high frequency oscillation part of the equation (4.20). This process can be achieved by a low pass filter in the real circuit.

$$v_{d1} = -Ri'_d + \omega_s Li'_q + v_d \quad (4.28)$$

$$v_{q1} = -Ri'_q + \omega_s Li'_d \quad (4.29)$$

Because only one resistor and one inductor are located between the GSC and the PCC, the transfer function of the inner current control loop can also be calculated simply. The entire inner current control loop is illustrated in figure 4.9.

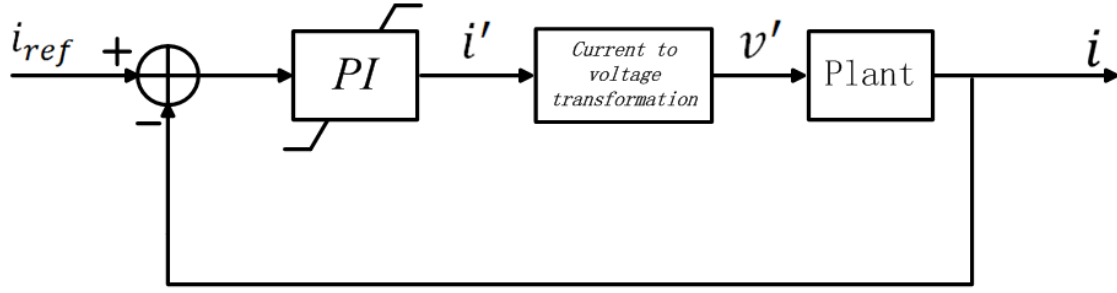


Fig. 4.9 Inner current loop control

#### 4.6.2 DC-Link voltage control loop

The DC-Link loop control strategy aims to stabilize the voltage over the DC-Link capacitor in an expected value, which can provide a reliable DC bus for the DC-DC converter in the EDVs side. Neglecting the power loss from the LCL filter and the GSC, the DC-Link control strategy can be preceded based on the power balance between the ac and dc sides of the GSC, as shown in equation (4.30). Assuming current  $i_{dc2}$  is the current injecting into the DC-DC converters in EDVs charging side (figure 4.8), equation (4.30) can be further transferred into (4.31). Finally, the transfer function (4.32) of the DC-Link voltage loop control can be calculated by ignoring  $i_{dc2}$  as interference.

$$v_{dc}i_g = v_d i_d + v_q i_q = v_d i_d \quad (4.30)$$

$$v_{dc} \left( C \frac{dv_{dc}}{dt} + i_{dc2} \right) = v_d i_d \quad (4.31)$$

$$G_d(s) = \frac{V_d}{V_{dc} \cdot C \cdot s} \quad (4.32)$$

The DC-Link voltage loop control scheme is shown in figure 4.10. Similar as the other feedback control scheme in the thesis, a PID controller is employed to minimize the error between measured dynamic voltage and reference.

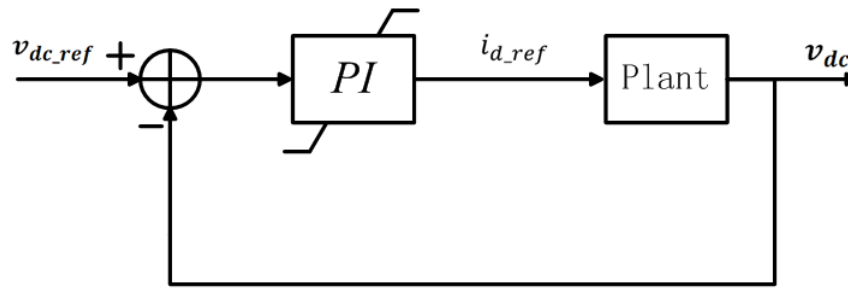


Fig 4.10 The DC-Link voltage loop control scheme

#### 4.6.3 Overall direct-current loop control strategy in grid side system

The main purpose of the grid side control system is to regulate the voltage across DC-Link capacitor and either of real/reactive power and the PCC voltage from grid side to the GSC. According to the equations (4.20), (4.21) and (4.22), these objectives can be archived by setting  $d$ -axis and  $q$ -axis currents as two references which are two inputs of direct-current vector control strategy. The frame of the direct-current vector control strategy is a nested-loop structure including a inner current control loop and a DC-Link voltage control loop. In the DC-Link voltage control loop, the PID controller receives the difference between the DC-Link voltage reference and the measured DC-Link voltage and outputs the tuning signal as the  $d$ -axis current reference of the inner current control loop. Therefore, the DC-Link voltage control can also be seen as an outer loop of the inner current control loop in  $d$ -axis current. On the other hand, the  $q$ -axis current can contribute to the reactive power or PCC voltage support control. In the reactive power control mode, the  $q$ -axis current reference is generated through a reactive power controller. In the AC system voltage support control mode, the  $q$ -axis current reference is generated through a PCC voltage controller, during which the GSC should generate a reactive power as much as possible depending on how much the PCC voltage drops. Finally, the structure of the direct-current vector control strategy is demonstrated in figure 4.11

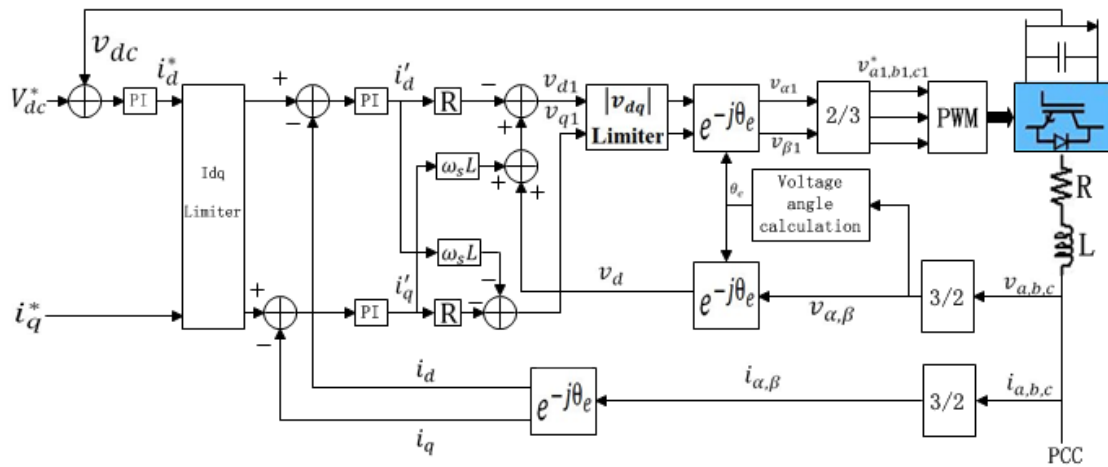


Fig 4.11 Direct-current vector control structure

Generally, the entire control strategy includes three steps:

First, since the equation (4.20), (4.21) and (4.22) demonstrate the relationship between DC-link capacitor voltage and  $d$ -axis current as well as the link between reactive power or PCC voltage and  $q$ -axis current, the two current references  $i_d^*$  and  $i_q^*$  are used to stabilize the  $d$ - and  $q$ -axis currents to a desired value, by which the voltage across DC-Link capacitor and reactive power can be controlled in an undirected way. Concretely, the  $d$ -axis current reference generated by PID controller mechanism is used to minimize the difference between the reference and actual voltage of the DC-Link capacitor. Meanwhile, the  $q$ -axis current reference is directly generated through equation (4.22) that aims to control reactive power.

Second, the inner current loop control scheme is employed for stabilizing the actual current of  $d$ -axis and  $q$ -axis into a desired level. The input error signal of the PID controller comes from the difference between the current reference ( $i_d^*, i_q^*$ ) we got at the previous step and the measured  $d$ - and  $q$ -axis current. According to dynamic input error, the PID controller unceasingly adjusts the output ( $i_d', i_q'$ ) and finally minimizes the error under a certain level.

Third, after the entire nested-loop control structure is designed, the step that transforms the current control signal into three-phase voltage control signal is still necessary since the GSC is based on the voltage control structure. According to relationship between grid side current and GSC output voltage shown as the equations (4.28), (4.29), the transformation can be achieved as shown in figure 4.11. Furthermore, the PID control mechanism is widely used in the grid side control system for the purpose of stabilizing the actual current or voltage into the expected value.

## CHAPTER 5

### EDVs SIDE CHARGER CIRCUIT CONFIGURATION OF THE CHARGING STATION

#### 5.1 Battery charging and discharging characteristic

Because of the harsh energy storage requirements of EDVs, which includes high energy density, high output power (density), long life, high charge–discharge efficiency, wide temperature range, minimal self-discharge, good load characteristics, good temperature storage characteristics, low internal resistance, no memory effects, fast charging, high degree of safety, high reliability, low cost and good recycle ability etc.[39], the energy storage system has been one of the biggest technology obstacles for the improvement of EDVs. Compared to other potential options of energy storage devices, such as fly wheel, super capacitor and fuel cells, the lithium-ion battery is known as the most feasible energy storage device for EDVs due to the high power and energy density, 80%-90% charge/discharge efficiency and no memory effects at present. In this chapter, the Li-ion battery is utilized for EDVs. Meanwhile, the DC-DC converter and corresponding control scheme are discussed.

As mentioned at chapter 2, the battery is a device that can store the electrical power into chemical energy and release the energy by chemical reaction [40, 41]. Due to the chemical working principle of batteries in nature, it is essential to charge and discharge batteries in a reasonable way, otherwise, the battery being one of the most expensive components of EVs would be damaged quickly.

### 5.1.1 Charging requirement

State of Charge (SOC) is a measured quantity that represents how much energy stored in the battery in the charging process. It is complicated to measure the SOC accurately since the measurement is disturbed by many factors, such as open circuit voltage, battery temperature, cycle life and charging/discharging rate. All of them are changed dramatically in different working environment and affected significantly by each other. Especially in the EDVs' application, the wide range of working temperature and ever-changing charging/discharging rate definitely improve the complicity of this process. Along with the increasing attention on the EDVs' application, accurate measurement of SOC for an EDV battery has become a hot issue again. Many researches focus on how to improve the SOC measurement accuracy with a more economical way. Generally, there are several approaches to estimate the SOC of the battery, including the discharge test approach, the Ah counting approach, the open-circuit voltage approach, the load voltage approach, the inherent resistance approach, the neural networks approach, and the Kalman filtering (KF) approach [42]. For a higher accuracy purpose, some of them are integrated together in some specific applications.

In terms of charging schemes of an EDV battery, three basic regimes are normally used for charging or discharging of secondary batteries, i.e., constant-current charging, constant-voltage charging, and taper-current charging [25]. Constant-current charging simply means that the charger supplies a relatively uniform current, regardless of the battery state of charging or temperature. This charging scheme helps eliminate imbalances of cells and batteries connected in series. However, determining the charging current level could be a challenging task. In general, a too low current cannot meet the charging speed requirement and a high charging current could easily catalyze an excessive damage at the end of the charging procedure by gasification of

electrolyte. On the other hand, constant-voltage chargers maintain nearly the same voltage input to the battery through the charging process, regardless of the battery's state of charge. Constant-voltage chargers usually cause a high initial current to the battery because of the greater potential difference between the battery and charger. In the taper-current charging method, the charging current decreases in proportion to the voltage rising of the battery [24]. This design is used to prevent the battery from the gasification and overheat caused by excessive charging current at the end of the charging process. However, due to the diversity between each of the batteries, it is hard to determine an appropriate charging current for a specific battery and decreasing rate of the charging current.

Concerning the advantages and drawbacks of each charging method, constant-current and constant-voltage methods are incorporated together during the battery charging control, which is also recommended by most of the Li-ion battery manufacturers. Charging schemes generally consist of a constant current charging until the battery voltage reaching the determined charge voltage, then constant voltage charging, allowing the charge current to taper until it is very small. During the charging process, recommended charging current is followed, which represents the ideal current at which the battery is initially charged (to roughly 70% of SOC) under the constant-current charging scheme before transitioning into constant-voltage charging mode [24]. In this way, not only the overheating phenomenon can be avoided in a certain extent, but the overcharge is also effectively prevented through the increasing open circuit voltage (OCV) of the battery.

### **5.1.2 Discharging scheme**

The purpose of discharging function for the EDVs charging infrastructure in this thesis is to realize V2G and V2V processes during the surge of electricity demand. Similar to the

charging procedure, the depth of discharge (DOD) is introduced to represent how much energy left during the discharging process. The ways to accurately measure the DOD are the same as the SOC strategies. Moreover, the over-discharge protection and a feasible discharging rate are also key points for the battery health in discharging process. An exaggerated discharging rate not only extremely diminishes the capacity of a battery, but also causes the overheat phenomenon that can damage a battery quickly. Thus, a constant current loop control is equipped to prevent the battery from the damage of discharge process in this thesis.

## **5.2 Structure of EDVs side system**

The structure of the EDVs side system is shown in the figure 5.1, in which a series of EDVs are connected with the DC bus through a number of DC-DC converters. To endow each of the EDVs with the independent power management functions (G2V, V2G and V2V), the isolated DC-DC converters and the corresponding loop control system are equipped in the integrated EDVs charging station. As a result, the EDVs charging station can take different functions according to the battery remaining capacity in the each of EDVs or the particular requirement of each EDV owner.

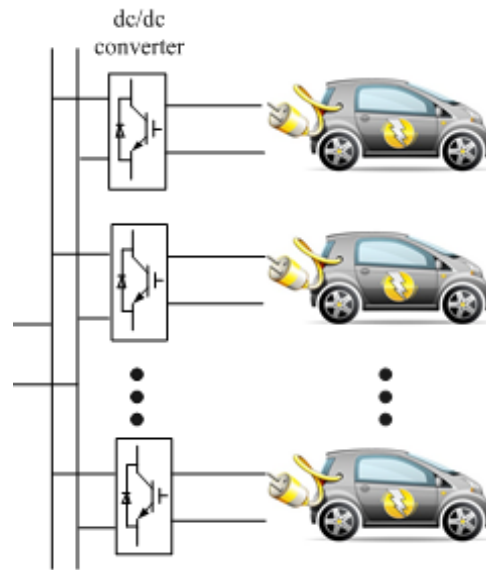


Fig 5.1 EV side system structure of EVs charging system

In terms of control strategy, there are two levels for the EDVs side system: including the EDV level and the centralized charging station level [8]. At the EDV level, each EDV is controlled by a DC/DC converter to implement the charge and discharge control of EDV batteries. At the central charging station level, the central control system sends out reference power signals to individual EDV charger by considering utility dynamic price information and EDV charge or discharge requirements, while the local EDV control system ensures that the reference power sent by the central control system is reached [43].

### 5.2.1 DC-DC converter structure

For processing the both charging and discharging functions by the proposed EDVs charging infrastructure, the DC-DC buck-boost converter is employed in this thesis as shown in figure 5.2. Similar to the GSC, the IGBTs are employed in the DC-DC buck-boost converter. The main application of the buck-boost converter is in regulated dc power supplies, where both

positive and negative-polarity outputs are desired with respect to the charging or discharging functions of EDVs in the charging station. The converter output voltage can also be either higher or lower than the battery voltage depending on the specific situation.

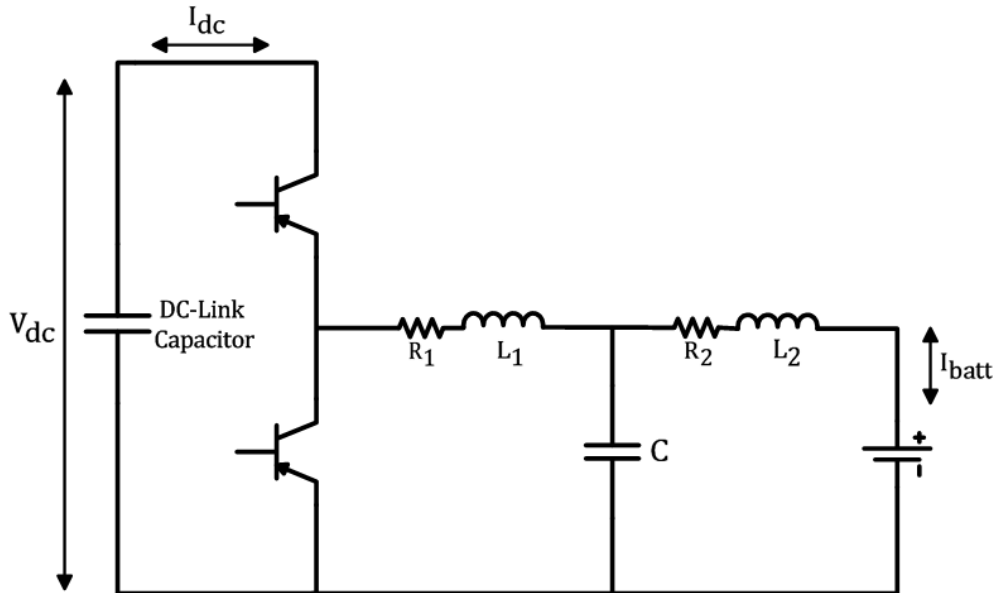


Fig 5.2 DC-DC bi-direction converter

### 5.2.2 LCL filter in EDV side system

Similar to the LCL filter in the GSC, a LCL filter is equipped in the EDV side system to reduce high frequency harmonic generated by the DC-DC converter in EDV side system. Referring to [44], a general procedure for the parameters of the LCL filter is explained below.

Generally, the purpose of LCL filter is processing the voltage generated by the DC-DC converter and yielding desired charging current with acceptable current ripple constraint for the battery. Therefore, the output voltage ( $u_1$ ) of the DC-DC converter and expected charging current ripple constraint should be decided before the design of the LCL filter. Since the output voltage ( $u_1$ ) of the DC-DC converter consists of equidistant pluses, it can be expressed by trigonometric Fourier series as shown in equation (5.1), in which the  $D$  represents switch duty cycle during the

steady state of system. In term of the charging current ripple constraint, the 10% peak to peak of the nominal current is seen as an acceptable value for the charging current ripple constraint which is shown as the equation (5.2).

$$u_1(t) = D \cdot V_{dc} + \sum_{h=1}^{\infty} \frac{2V_{dc} \sin(h\pi \cdot D)}{h\pi} \cos(h\omega_{sw}t) \quad (5.1)$$

$$\Delta \hat{i}_{batt} \leq 0.05 I_{batt,n} \quad (5.2)$$

Next, transfer functions between currents in inductors  $L_1$ ,  $L_2$  and output voltage ( $u_1$ ) of the DC-DC converter are calculated in this step respectively. The equation (5.3) representing the state-space description of the LCL filter is derived from the figure 5.2, in which  $i_1$  and  $i_2$  stand for the current of inductors  $L_1$  and  $L_2$  while  $u_1$  shows the DC-DC converter output voltage and  $u_c$  reveals the voltage across the LCL capacitor  $C$ . Then, the transfer functions from converter output voltage  $u_1$  to the current  $i_1$  and  $i_2$  are derived through equation (5.3) as shown in equation (5.4), (5.5), where the resistors  $R_1$  and  $R_2$ , which are connected with inductors  $L_1$  and  $L_2$  in series separately, are neglected.

$$\frac{d}{dt} \begin{bmatrix} i_1 \\ u_c \\ i_2 \end{bmatrix} = \begin{bmatrix} -\frac{R_1}{L_1} & -\frac{1}{L_1} & 0 \\ \frac{1}{C} & 0 & -\frac{1}{C} \\ 0 & \frac{1}{L_2} & -\frac{R_2}{L_2} \end{bmatrix} \begin{bmatrix} i_1 \\ u_c \\ i_2 \end{bmatrix} + \begin{bmatrix} \frac{1}{L_1} & 0 \\ 0 & 0 \\ 0 & -\frac{1}{L_2} \end{bmatrix} \begin{bmatrix} u_1 \\ V_{batt} \end{bmatrix} \quad (5.3)$$

$$G_{i_1}(j\omega_{sw}) = \frac{(S^2 - \frac{1}{L_2 C}) \frac{1}{L_1}}{S(S^2 - \frac{L_1 + L_2}{L_1 L_2 C})} \quad (5.4)$$

$$G_{i_2}(j\omega_{sw}) = \frac{\frac{1}{L_1 L_2 C}}{S(S^2 + \frac{L_1 + L_2}{L_1 L_2 C})} \quad (5.5)$$

In order to obtain the attenuation at the switching frequency, Laplace operator in the equations (5.4), (5.5) is replaced by  $j\omega_{sw}$  of Fourier transform. The result is given by equation (5.6), (5.7).

$$G_{i_1}(j\omega_{sw}) = \frac{(\omega_{sw}^2 - \frac{I}{L_2 C}) \frac{I}{L_1}}{\omega_{sw} (\omega_{sw}^2 - \frac{L_1 + L_2}{L_1 L_2 C})} \quad (5.6)$$

$$G_{i_2}(j\omega_{sw}) = \frac{\frac{I}{L_1 L_2 C}}{\omega_{sw} (\omega_{sw}^2 + \frac{L_1 + L_2}{L_1 L_2 C})} \quad (5.7)$$

Then, for obtaining the specific value of the inductors and capacitor of the LCL filter, two additional conditions are necessary to be decided. First, the filter capacitor  $C$  is assumed as same value as the capacitor of the grid side LCL filter. Second, in order to solve the equations (5.4) and (5.5), one more factor  $x$  is introduced which represents the relationship between the current ripples between inductor  $L_1$  and  $L_2$  as shown in equation (5.8). According to reference [44], the factor  $x$  is assigned as 3 which implies the current ripple of the inductor  $L_1$  is equal to 3 times of the current ripple in the inductor  $L_2$ .

$$|G_{i_1}(j\omega_{sw})| = x \cdot |G_{i_2}(j\omega_{sw})| \quad (5.8)$$

Finally, the solution of the LCL filter parameters can be calculated by equations (5.9) and (5.10).

$$L_1 = \frac{2V_{dc}}{x\omega_{sw}\pi\Delta\hat{i}_{batt}} + \frac{x+I}{x\omega_{sw}^2 C} \quad (5.9)$$

$$L_2 = \frac{x+I}{\omega_{sw}^2 C} \quad (5.10)$$

### 5.3 EDV side control scheme

Both constant-current and constant-voltage control schemes are investigated in the EDV side control scheme. The two control techniques are then integrated and incorporated together to accomplish different battery charge and discharge requirements (Figure 5.3). In figure 5.3, the switch block passes through the top input or the bottom input based on the value of the SOC control input in the middle.

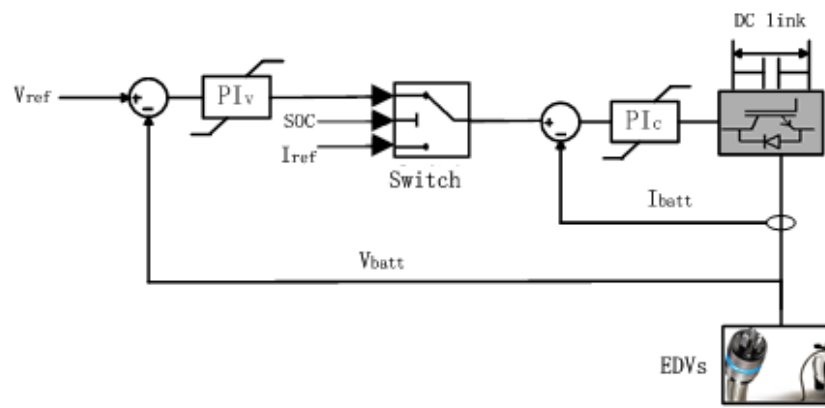


Fig 5.3 Constant-current and constant-voltage control mechanisms for charging and discharging of EV battery

If the switch is in the bottom position in figure 5.3, then, the system operates in the constant-current control mode, in which the  $PI_c$  block stands for the constant-current controller. The input signal to the controller is the error signal between the reference and measured battery current, and the output of the controller is the duty-ratio applied to the dc/dc converter for battery charge and discharge control. The reference current can be either positive or negative. Assume that the current flowing into the battery is positive. Then, if the reference current is positive, the system implements constant-current charging control function; if the reference current is negative, the system implements constant-current discharging control function.

The transition from current control to voltage control for charging is determined by the SOC. When the SOC is below 70%, constant-current charging mechanism is employed; when the SOC is over 70%, the system switches to constant-voltage charging mechanism. For smooth transition from the current to voltage control, the initial value of the voltage controller  $PI_v$  should have the same value of the current reference before the transition happens. For discharging control, constant-current control mechanism is employed. The power provided by the battery to the grid or other EDVs can be regulated by adjusting the reference discharging current.

## CHAPTER 6

### REAL TIME SIMULATION IMPLEMENTATION

#### 6.1 Introduction of Real time simulation

Simulation tools have got a rapid evolution from the analog simulators at the beginning to the digital simulators in the past decades. Unlike the simulators with limited capability and high cost at the early stage, the modern simulators not only possess more powerful capability that can solve more complicated problems in less time, but also become affordable by wider users and make digital simulators available in more areas. At present, the digital simulators have been used widely in a number of industries. Especially, the real-time simulation, based on automatic code generation, has played vital role in many engineering field and applications, such as aircraft flight control design & validation, industrial motor drive design, complex robotic controller design and power grid statistical protection tests. [45]

#### 6.2 Functions of Real-time simulations

The real-time simulation can be defined as a virtual model established by computer on the basis of the objective physical system. It can work at the same rate as actual "wall clock" time, namely, the actual physical time. With this capability in nature, a real-time simulator can bring benefits to industrial design in many aspects. Generally, the functions of the real-time simulation can be divided into three categories: [46]

- Rapid control prototyping (RCP)

- Hardware-in-the-loop (HIL)
- Pure simulation ( PS)

In the RCP function, a proposed controller archetype is established into a virtual model by a real-time simulator and connected with physical plant by I/O port. Instead of testing a physical controller, a virtual model provides a more flexible, faster and more economical way for controller debug. Since the controller prototype is a virtual model implemented by the simulator, any tuning and modification can be easily completed by a few mouse clicks. Especially in a very big system, such as a large power grid or an aircraft, the virtual controller archetype can be tested by external physical plant and make adjustment accordingly. On the contrast, it will be a nightmare that some problems are found after the entire physical prototype is established.

The HIL simulation aims to provide an effective platform for developing and testing physical controller. When the current hardware is much more complicated than before, the complexity of the embedded system, which is designed to control hardware, also has a great improvement. Through HIL simulation, the designed controller no longer needs to wait for a physical plant to write or test code. The plant is able to be replaced by a virtual model established by a real-time simulator, in which the testing can include the simulation for large versions of the plant, such as a high power generator. Usually, it is risky to test a controller in a large physical plant. Especially, testing the physical controller in some extreme case, such as simulation of over burdening, would likely destroy a physical plant [48]. For these facts, the HIL simulation is introduced to work as an effective platform in a controller testing, especially for the case of some very complicated plants which are hardly achieved in physical model.

Unlike RCP and HIL involving physical model in test, PS mode employs virtual models to take the places of both controller and plant in the real-time simulation. Since there is no input

and output signals between virtual model and physical model, the signal loss existed in RCP and HIL is able to be eliminated in PS mode. As a result, the test in PS mode will be more accurate than RCP and HIL mode without the influence of signal loss. Moreover, PS mode can also provide a faster simulating speed than real-time with no impact on the validity of results. Because of the higher simulating rate and more powerful calculation capability than other simulators, the design period of a controller can be effectively shortened.

### 6.3 Time-step in real-time simulation

Simulation can be simply defined as an imitation of the operation in a real-world process or system over time [47]. In order to simulate a system in a valid way, it is necessary to set every components of the system in an appropriate rate and guarantee signals transferring between subsystems with a correct timing. In a real-time system, a constant duration is decided as a discrete time interval in advance. The processor of a real-time simulator has to repeatedly complete three procedures in each predetermined time interval as shown in figure 6.1. The processor first receives input data from other systems and then computes all the functions and equations representing a system in accordance with the data. After the computation is completed, the result will be written and output from the processor. All these three steps should be finished during the predetermined time interval which is normally known as fixed-step simulation.

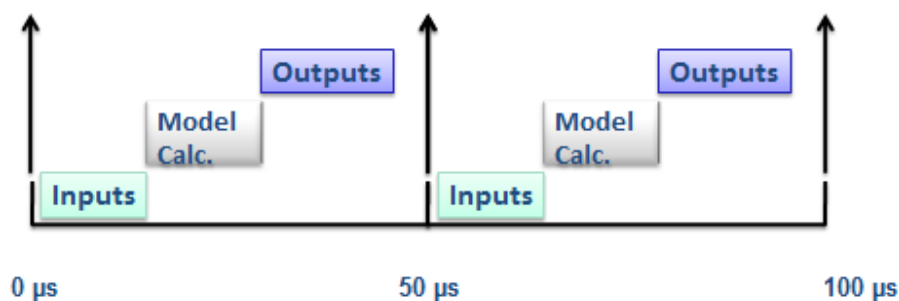


Fig. 6.1 Fixed time step simulation

Depending on the different complicity of a virtual system, the time spent on calculating functions and equations of the virtual system could be variable. Once the time step of a simulation is determined in advance, the actual time that a processor takes could be either longer or shorter than the time step. In order to make sure that a real-time simulation works validly, a simulator has to take less time than the predetermined time step, otherwise, the simulation would be working on an inaccurate state which is called “overrun”. Figure 6.2 illustrates the overrun phenomenon, in which the predetermined time step is too short and the simulator spends longer time on computation than the predetermined time interval. In this case, the simulator not only occupies the first time step, but also takes part of the second steps. Then all the tasks of simulator in the second time-step, including signal input, computation and result output, are omitted. Meanwhile, the simulator directly jumps over the rest of the idle time step and waits until the clock ticks to the next time-step. Especially in the HIL and RCP modes of real-time simulation, the simulator has to have a same operating rate as the actual physical devices since the simulator aims to swap data through inputs and outputs (I/O) with externally physical devices. If a simulator cannot complete the three tasks in time, which may be caused by a too complicated virtual system or lack of computation capability in simulator, the real-time simulation result is considered erroneous.

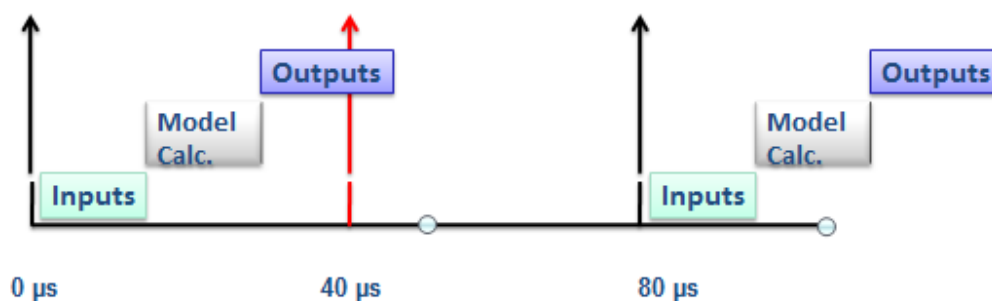


Fig. 6.2 overrun phenomenon in real time simulation

## 6.4 RT-LAB for real-time simulation

As a real-time simulation platform, the RT-LAB software is used to achieve high-fidelity plant simulation control system prototyping, and embedded data acquisition and control. Meanwhile, its distributed processing capability also allows users to quickly convert Simulink™ or Systembuild™ models to high-speed, real-time simulations, over one or more target PC processors. It is flexible enough to be applied to the most complex simulation and control problem no matter whether it is for real-time hardware-in-the-loop applications or for speeding up model execution, control and test. [48]

The real-time simulation aims to get smaller maximum time step and maintain the simulation accuracy to a certain level with fixed-time step solver. Comparing with the typical variable-step solvers, the utilization of the fixed-time step solver can lead to some inaccuracies because there is no built-in accuracy check within the solvers [49]. In order to realize complicated electrical systems in real-time simulation and improve accuracy of the result, the RT-LAB Electrical Drive Simulator comes with some special Simulink-based modeling tools, such as ARTEMIS and RT-Events, which permits the real-time simulation of an electrical system at practical time step of  $10\mu s$ .

### 6.4.1 ARTEMiS toolbox

ARTEMiS works as a plug-in blockset under the SimPowerSystem and helps to improve distributed simulation of power systems over multiple processors. Other than normal simulations whose objective is to minimize total simulation time or the smallest average simulation time step, a real time simulation is proposed to get a smaller maximum time step to fulfill the operating rate of the external physical devices in the simulation while keeping the accuracy in a certain extent. For these purposes, Artemis is introduced to satisfy real-time simulation requirements in several

aspects [49]. First, ARTEMiS can extend the range of time step to achieve both speed and precision for a specific real-time application. Second, some oscillations caused by network switching are hardly damped under minimum hardware limits. To solve this fact, ARTEMiS solvers' good damping properties are able to damp the spurious oscillations efficiently. Third, in applications where some underdamped or high frequency components, relative to the fastest possible sampling time, must be taken into account, ARTEMiS improves the precision of those components comparing to the trapezoidal or Tustin methods. Moreover, ARTEMiS also offers a new solver called State-Space Nodal which combines the accuracy potential of state-space methods with the natural ability of the nodal approach to handle circuit with a large number of switches.

#### **6.4.2 RT-Events toolbox**

Similar to ARTEMiS, RT-Events is another blockset that can be used with the Simulink software and that enables the simulation of event-based systems that comprise continuous- and discrete-time subsystems whose dynamics changes due to discrete events [50]. Generally, RT-Event is introduced to solve following problem encountered in the simulation of event-based systems. During a simulation, errors would be introduced by the situations that some switching events may occur between the sampling instances or multiple events occur in a single time step. Although the standard Simulink blocks are able to compensate the errors through the variable-time step solver, it is still inaccurate due to the lack of the timing information. This problem would be worse when the fixed-time step in the order of 10-100  $\mu s$ . In the terms of the RT-Event, although the switching signal is updated in every sampling instant as same as standard SimPowerSystem, the accuracy of simulation result is highly increased for the same time-step

since the switching and state transition information are concurrently kept in the time stamp as shown in figure 6.3.

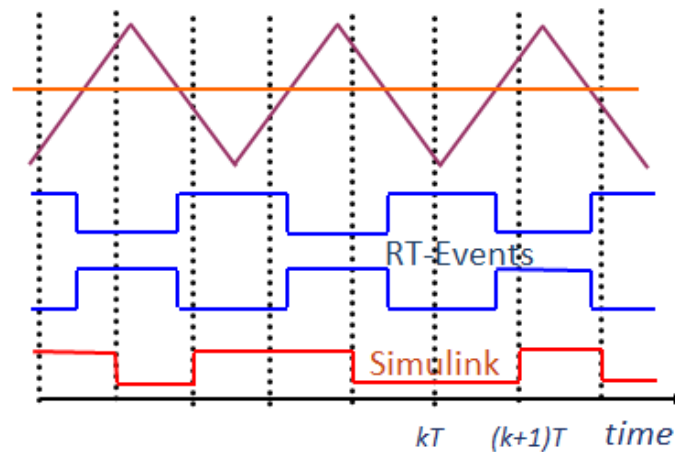


Fig 6.3 Comparison between RT-Event and Standard Simulink

#### 6.4.3 From Simulink based design to Real-Time module by RT-Lab

RT-LAB uses Simulink to define models and corresponding parameters which will be executed by the real-time multi-processing system. After the model of integrated EDVs charging station is implemented in Matlab/Simulink, several more steps have to be completed to realize the real-time model in the RT-Lab software and hardware.

1. Regroup into subsystems
2. Add the OpComm block(s)
3. Maximize parallel execution and state variables
4. Set the real-time parameters
5. Run offline

The interface of RT-Lab is shown in Figure 6.4. In order to regroup the original Simulink model into several subsystems and add necessary blocks on it, RT-LAB software permits

customer to open the model through Simulink under RT-Lab environment. This step can be simply operated by clicking the button with Matlab icon located at toolbar at left top of figure 6.4.

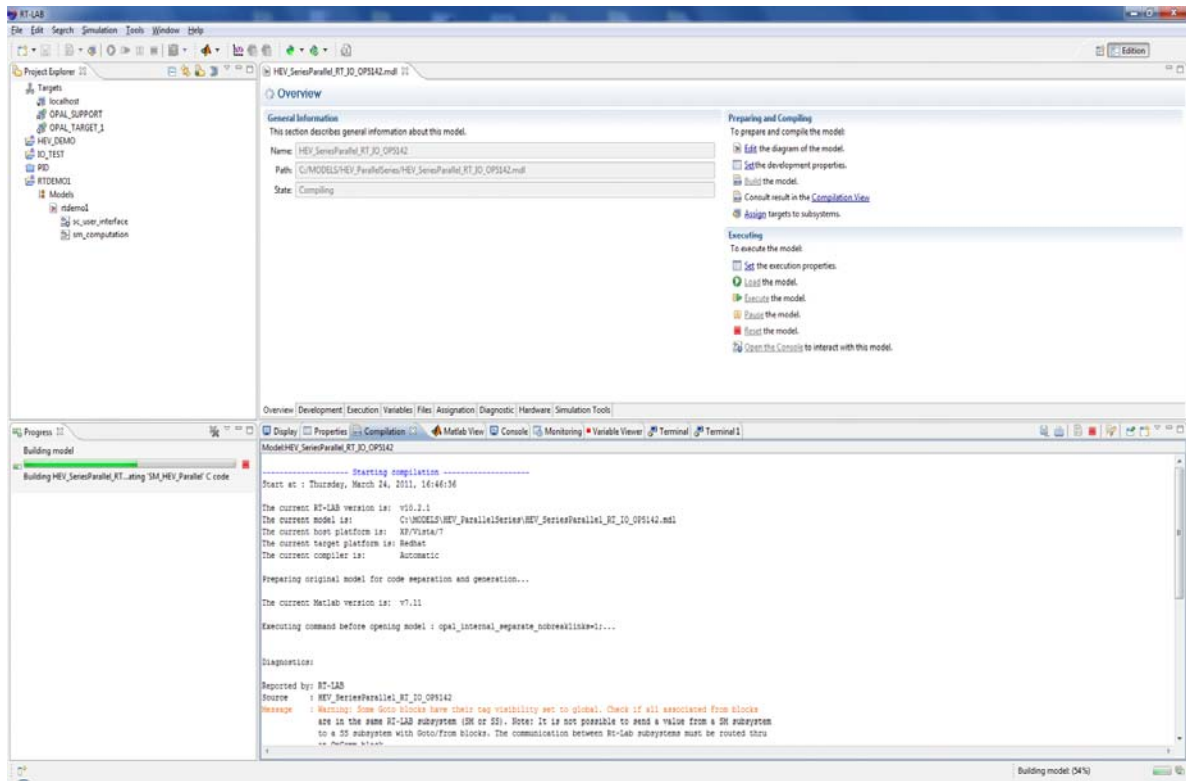


Fig. 6.4. Interface of RT-LAB software

According to the rules of RT-LAB software, a Simulink model is required to be divided into several subsystems based on different states of subsystems. First, every real-time simulated model has to have one and only one master subsystem. Some important and complicated computational elements of the model, such as the mathematical operations, the I/O blocks and the signal generators, are recommended to locate in this subsystem, since this subsystem has the highest priority than other subsystems in computation. On the other hand, a number of slave subsystems are also allowed in a real-time simulating model. The main purpose of both master and slave subsystems are to distribute the computation task into different CPUs. Depending on the demand of computation and the number of CPUs, users can establish several slave

subsystems or none of them. Third, to settle scopes, displays and switches, a console subsystem is introduced in RT-Lab software. None of CPUs is distributed on the console subsystem, because this subsystem is merely located in the host computer and aims to reflect results of the real-time simulation. Figure 6.5 illustrates the status of a master subsystem, a slave subsystem and a console subsystem. The blocks at the left hand of the figure respectively represent a master subsystem and a slave subsystem, while the right block is a console subsystem. When the real-time simulation is operating, the calculations in the master and slave subsystems are located at the different CPUs of the target computer. On the other hand, the console subsystem will stay at the host computer and be in charge of the result display and some parameters adjustment. Since every subsystem has to be distributed into corresponding processors in the real-time simulation, no mathematical content can be found in the top-level of the model. In addition, a prefix to all the top-level subsystem is required to allow RT-LAB distinguishing the status of them, such as master subsystem, slave subsystem and console subsystem. As shown in figure 6.5, the names of the master subsystem, slave subsystem and console subsystem separately start with “SM\_”, “SS\_” and “SC\_”.

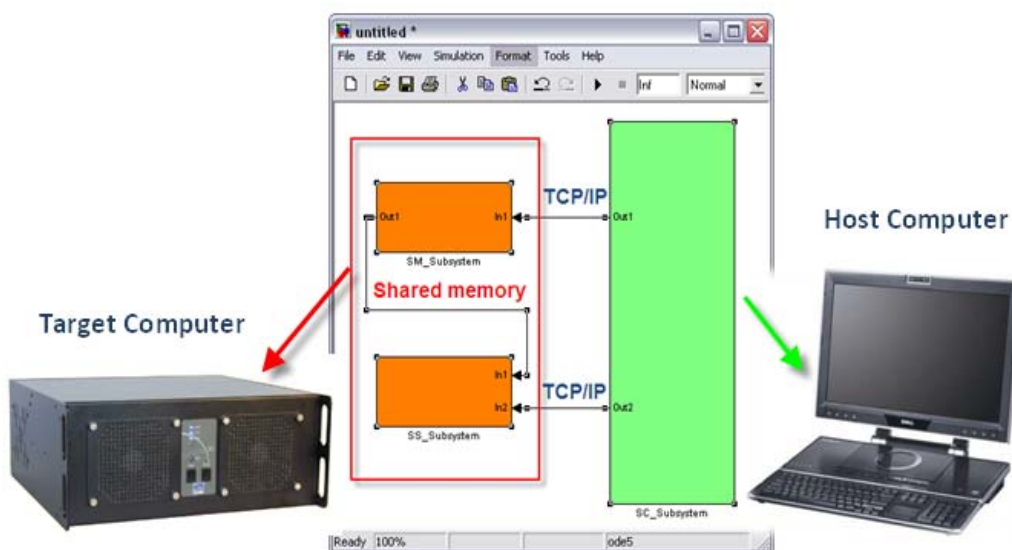


Fig. 6.5 Status of different kinds of subsystems for RT-LAB

In the next step, the “OpComm” block is equipped in each subsystem of the model. Technically, the communication between any two subsystems, regardless of the console or computation subsystems plays a vital role in real-time simulation. The “OpComm” block is used in RT-LAB to enable and save communication setup information. According to RT-LAB rules, all subsystems inputs must first go through an “OpComm” block before any operations can be done on the signals.

Step 3 aims to maximize parallel execution and state variables. Again, the purposed model is divided into several subsystems and processed separately in multiple CPUs in RT-LAB. In order to synchronize the execution in every subsystem and achieve the fastest processing speed, RT-LAB introduces the “integrator” and the “memory” blocks to help parallel execution and synchronized communication between subsystems. The “integrator” or the “memory” blocks have to be located at the output of every subsystem as shown in figure 6.6.

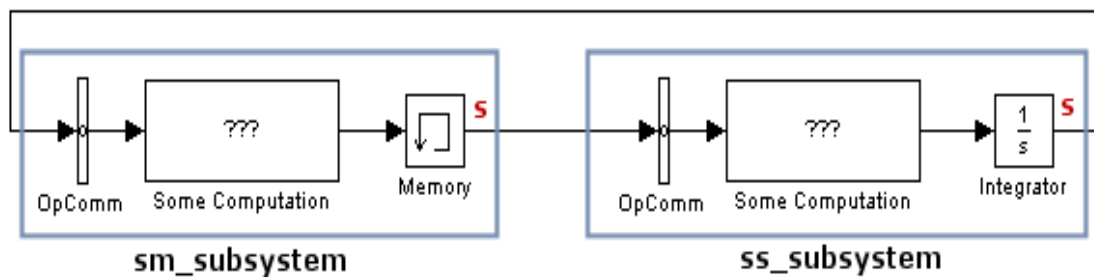


Fig. 6.6 Maximum parallel execution by “integrator” or “memory” blocks

After the modification of the model in previous steps, some parameters have to be set in advance to make the model accessible in real-time simulation. Figure 6.7 presents the interface of RT-LAB which is used to set a number of configuration parameters. Among these parameters, the time-step mode and corresponding parameters are required to be set before execution. These parameters are labeled by circle in figure 6.7. It is mentioned that the real-time simulation can

only run in the fixed-step mode, so the solver type has to be set on fixed-step in the “type” option of the interface. Moreover, regarding to the fixed-step size, the sampling time of real-time simulation is equal to 50us in this thesis. For the “stop time” option in figure 6.7, this parameter does not apply to the simulation duration, but aims to set the working time of console subsystem. This option is normally set to “inf” since it is expected to run the consoles as long as the real-time simulation.

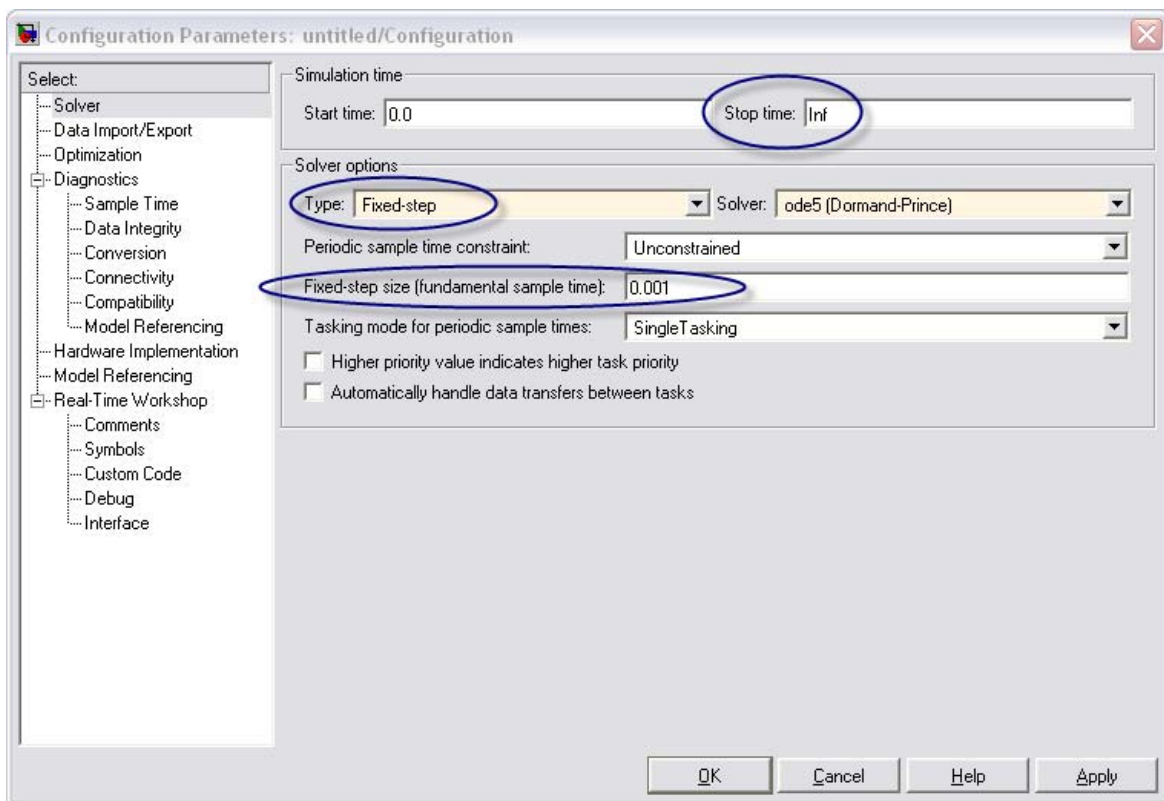


Fig. 6.7 Interface for configuration parameters in RT-LAB

### 6.5 Computational Experiment System of EDVs Charging Station for Real-Time Simulation

To evaluate different control functions of the charging station, a computational experiment platform of the integrated GSC and ESC system of EDVs charging station is developed. The computational experiment system is developed by using power converter

detailed switching models in MatLab SimPowerSystems and RT-Lab power converter models. The advantages of this computational experiments generally include: 1) flexibility to access and study any nodes in a system that are practically measurable or immeasurable; 2) ease modification of any control or computing algorithms to study system performance both within and beyond physical system constraints; and 3) flexibility to simulate a complex system in different ways while hardware measurements are normally limited to one approach, i.e., transient data measured over time.

The computational experiment system mainly includes three parts: a EDV battery module, a power converter module, and a control module. Since the experiment system is implemented by using the RT-LAB real-time simulation technology which is able to distribute the entire system into several parts and calculate each of them through different CPUs, the EDVs charging station system is divided into several subsystems as shown in figure 6.8. The four subsystems in figure 6.8 separately represent a Grid Side System (left) and three EDVs side charging systems (right). The Grid Side System is labeled as master subsystem, because the calculation in this part is more complicated than the other subsystems. On the other hand, the other three subsystems, which respectively represent three charging EDVs batteries and the corresponding EDVs side charging systems, are labeled as three slave subsystems. The console subsystem isn't shown in this figure, since there is no mathematical calculation in it.

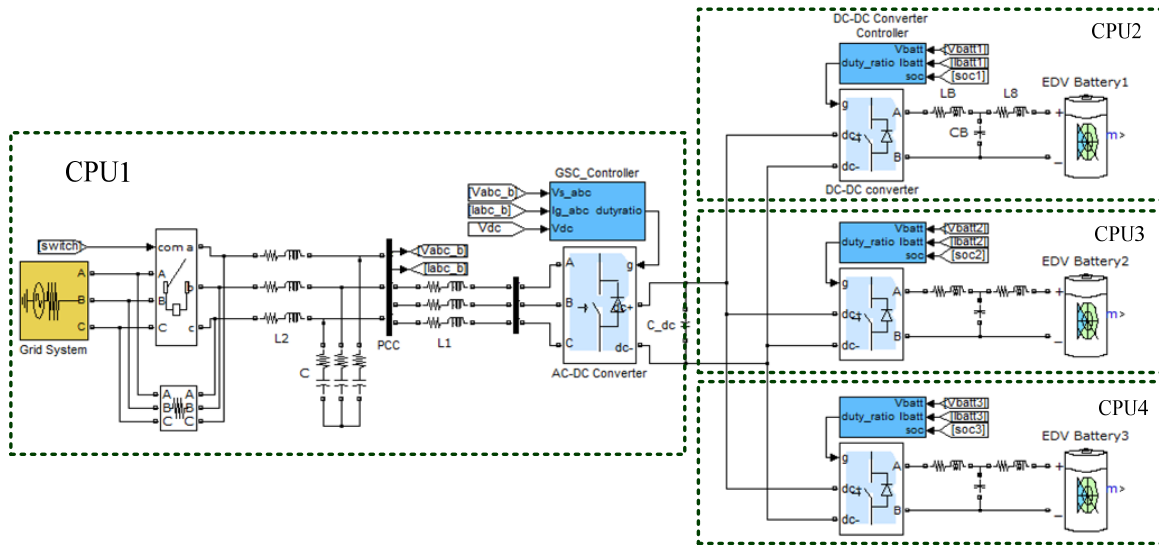


Fig. 6.8 Real-time simulation structure of converter system for EDV charging station

It is well known that the size of state-space matrices depends on the number of states or number of inputs and outputs of a system. In the case of a real-time simulation where the sampling interval is strictly limited, an over large state-space matrix not only puts more pressure on CPUs, but also may causes memory overflow that would further generate errors in result. Hence, RT-LAB software employs a number of decoupling tools from ARTEMiS blockset to solve this problem. The decoupling tools are able to divide a big matrix into multiple smaller state-space matrices which make the computation easier and faster for the CPUs of simulator. In another word, the decoupling tools from ARTEMiS library make the parallel simulation available by multiple CPUs in real-time simulation. In this thesis, the “StubLine block” from ARTEMiS library is equipped between subsystems. It is also important to note that the decoupling tools are not an option here. Without them, the subsystems cannot be processed under multiple CPUs simulator.

## 6.6 Grid side system module of the integrated EDVs charging system

The block labeled with CPU1 of figure 6.8 illustrates the structure of the grid side system. This block is set as a master system and consists of 1) a variable amplitude and frequency AC voltage source representing the power grid, 2) a switch and corresponding bypass for three-phase resistors, 3) a three-phase LCL filter, 4) a three-phase grid side switch-model AC-DC converter, 5) a DC-link capacitor. Moreover, the three-phase AC voltage and current are measured at the PCC in the grid side system for realization of control strategies, such as DC-link voltage control, reactive power control or voltage bus control.

### 6.6.1 Module for three-phase axes to $dq$ -axes frame reference transformation

In the grid side system, the inputs of control scheme are the measured three-phase voltage and three-phase current at the PCC, as well as the voltage of the DC-link capacitor. To realize the direct-current control scheme, the three-phase voltage and current should be transformed into  $dq$  axis frame. The blocks used to transfer three-phase  $abc$  axes to  $dq$  axes frame is shown in figure 6.9 below. Specifically, the “theta” block is used to calculate grid voltage phase position in equation (4.16), which is a critical element for obtaining  $dq$  rotating reference frame. The main calculations, Clarkson transformation and Park transformation, are located in the block “abc\_dq”. Then through two “mean value” blocks, the currents on  $dq$  rotating reference frame are obtained.

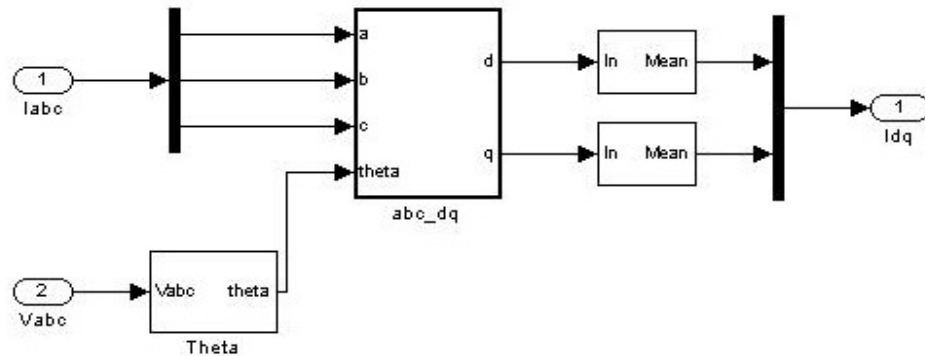


Fig. 6.9 Module for three-phase axes to  $dq$  axes frame reference transformation

### 6.6.2 Directed-current control modules for GSC

The PI controller used in the control system aims to get expected control signal through unceasingly tuning the error between measured value and reference. The currents on  $dq$  axes reference frame ( $I_d, I_q$ ), which are obtained from section 6.6.1, are used as the inputs of directed-current system module and subtracted by the corresponding current references of the PI controller scheme. The module of directed-current control strategy is shown in Figure 6.10.

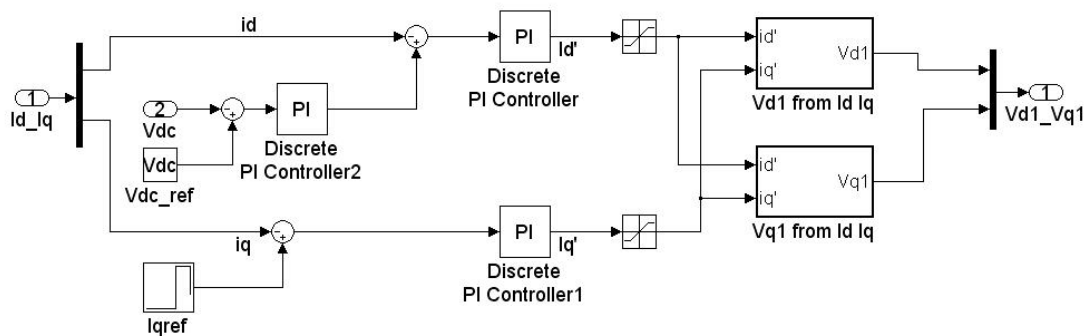
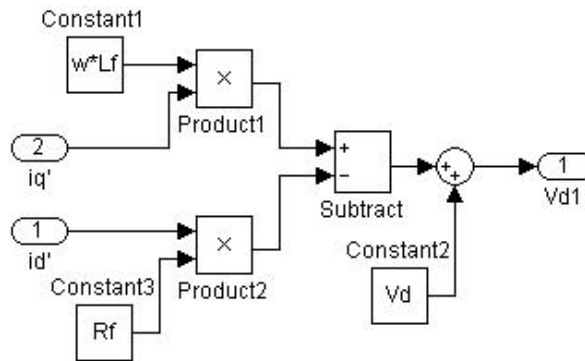


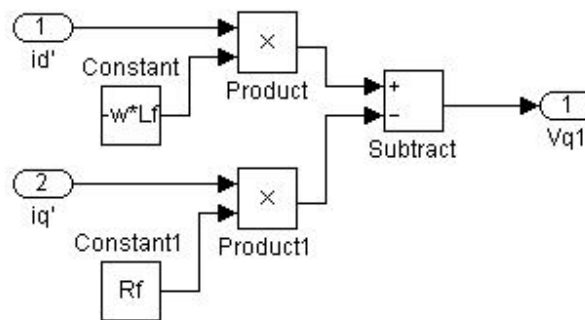
Fig. 6.10 Directed-current control module

The  $d$ -axis current reference is generated by comparing the difference of actual and desired DC-link voltage, while the  $q$ -axis current reference is introduced to get desired reactive power at

PCC. Since the GSC is a voltage based converter, the current signals outputted from PI controllers are still need to transform into  $dq$ -axes voltage signals. According to equations (4.28) and (4.29), this procedure is achieved in blocks “ $V_{d1}$  from  $I_d I_q$ ” and “ $V_{q1}$  from  $I_d I_q$ ”. The interior structures of these two blocks are presented in figure 6.11.



(a)  $V_{d1}$  signal generation in proposed control system



(b)  $V_{q1}$  signal generation in proposed control system

Fig. 6.11  $V_{d1}$  and  $V_{q1}$  signals generation blocks in proposed control system

## 6.7 EDVs side system module of the integrated EDVs charging system

### 6.7.1 EDVs side power path module

The three blocks labeled with CPU2, CPU3 and CPU4 in figure 6.8 present EDVs side system, including three batteries of EDVs and corresponding EDVs side charging system. Each

of them stands for a slave subsystem with same status and similar structure in the real-time simulation. The power path of each of the EDV side charging system consists of 1) a buck-boost DC-DC converter from RT-Event library, 2) a LCL filter for high frequency oscillation reduction, 3) a battery model. Specifically, the battery model for each EDV has adopted lithium-ion battery, which is available from Matlab SimPowerSystem library. These three battery models are connected with the DC bus in parallel and exchange power with the grid or each other through the DC bus. To provide a high quality charging voltage to the three batteries, a LCL filter is introduced between the DC/DC converter and the battery in the each subsystem.

### 6.7.2 EDVs side control system

Figure 6.12 shows the module of EDVs side control system. The battery charge and discharge control of the EDV battery is managed with careful consideration of the SOC, and voltage and current of the battery. Major measurements of the EDV battery include power, current, voltage and SOC of each battery, which works as input of EDVs side control system. The power sign convention is used, i.e., power absorbed by the battery from the DC bus is positive. The blocks " $V_{ref}$ " and " $I_{ref}$ " are used to provide voltage and current references for charge and discharge procedure. Meanwhile, the "switch" block aims to choose corresponding control path in the module. In the constant voltage charge case, the expected charging voltage reference is applied to battery charging control procedure.

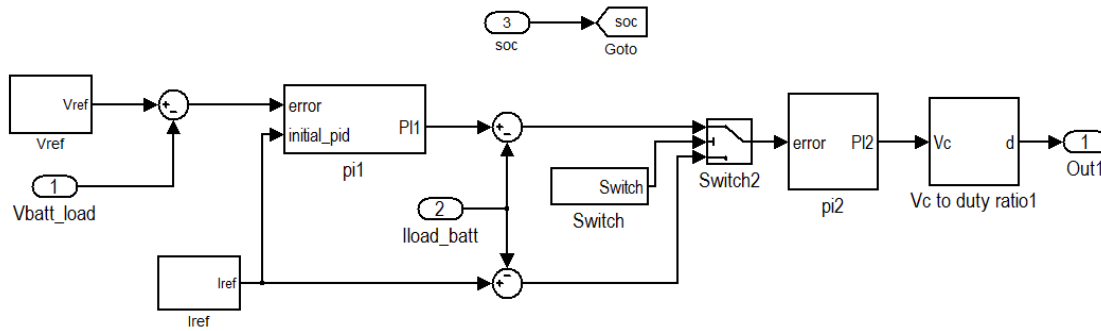


Fig. 6.12 EDVs side control system module

The first PI controller receives the difference between measured charge voltage and reference and outputs the tuning voltage signal. Then, the inner current loop is realized by the second PI controller. The output signal from “PI1” block is subtracted by the measured charging current and then processed by the second PI controller. As mentioned in Chapter 5, the purpose of the inner current loop is to obtain a more stable charging current when the constant voltage charge mode is applied. When the SOC reaches 70% in charge process, the switch will break the constant voltage control path and switch to the constant current charge path. During this process, the constant current reference is applied until the charge process is completed. On the other hand, the “switch” block will switch to the constant current control path during the discharge process, in which the current reference is set as a negative value for providing a discharge command to the DC-DC converter. After the final tuning signals generated from the second PI controller, the tuning signal is normalized in block “ $V_c$  to duty ratio1” and further transformed into PWM control signals which is required by the EDVs side converter.

## CHAPTER 7

### EDV CHARGING STATION CONTROL EVALUATION IN TRANSIENT CLOSE-LOOP ENVIRONMENT

To evaluate the charge/discharge control schemes of the integrated EDVs charging station mentioned before, a number of simulations are operated over the real-time simulation system in this chapter. Since either grid side AC system reactive power or PCC voltage is able to be controlled by  $q$ -axis current reference, a reactive power compensation mode and a bus voltage support mode are simulated separately in the Section 7.1 of this chapter. In addition, the G2V, V2G and V2V mode simulations of the integrated EDVs charging station can also be realized through the DC bus established by the DC-Link capacitor and the DC-DC converters equipped to each of EDVs. In section 7.2, the result and analysis about G2V, V2G and V2V simulations are presented, respectively.

#### 7.1 Reactive Power Control and PCC Voltage Compensation in Grid Side System

##### 7.1.1 Charge/Discharge and Grid Reactive Power Controls

The case study of the grid reactive power control and battery charge and discharge control for one EDV is presented by figure 7.1, 7.2 and 7.3, in which a number of parameters including battery charging current/voltage, SOC, DC-Link voltage, currents of  $dq$ -axis ( $I_d, I_q$ ) and reactive power are illustrated separately. As described in Chapter 5, a CC/CV charging scheme is employed for EDVs charging process. At the beginning, the SOC of battery is set below 70% in advance. Then, a 20A constant current charging is applied between  $t=3s$  and 5s. In order to evaluate the performance of EDVs charging station in different constant charging current, the

charging current leaps into 30A at  $t=5s$  (figure 7.1a). When the SOC reaches 70% around  $t=9s$ , the battery control automatically turns to constant voltage mode. As shown in figure 7.1b, the charging current reduces quickly and an acceptable oscillation is generated around  $t=9s$ . Correspondingly, the charging current will not follow current reference anymore. Technically, when the constant voltage charge procedure is on, the measured charging current ought to be lower than the constant current period and unceasingly decrease to prevent battery from gasification and overheating phenomenon (figure 7.1a). At  $t=14s$  a command is issued with a current of -10A. From this moment, the EDV enters discharging process.

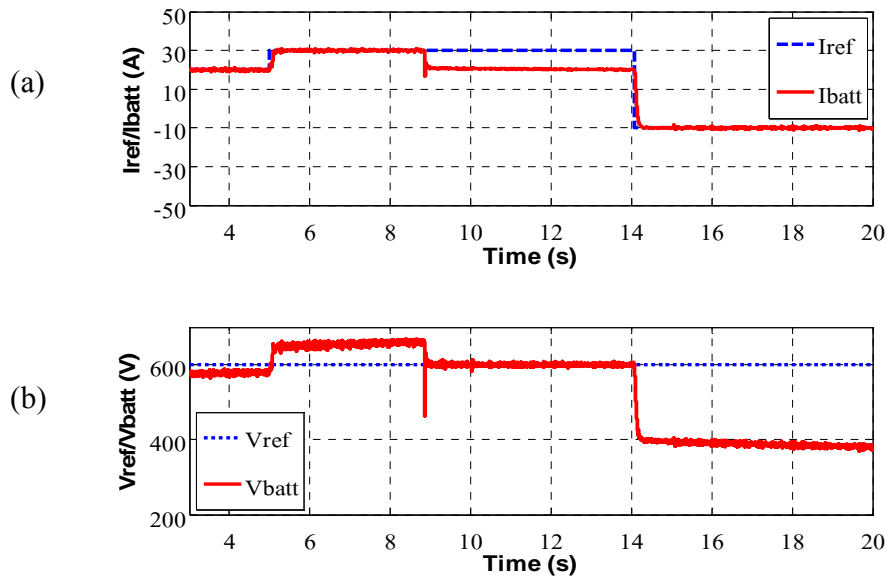


Fig. 7.1 Charging current and voltage during charge/discharge and reactive power control

The response of SOC and DC-Link voltage is illustrated in figure 7.2. During the charging state between  $t=3$  and  $t=14$ , the SOC of the battery keeps growing. Specifically, referring to the different charging current or voltage, the growth curve of the SOC of battery shows various slope. Since the charging current leaps from 20A to 30A when the SOC reaches 69.5%, the slope of growth curve of SOC under 30A charging current is clearly bigger than the

case of 20A charging current. After the SOC reaches 70%, the charging process enters constant voltage scheme. During this period, the SOC growth rate slows down. Differing with the constant current charging scheme, the charging rate of the constant voltage scheme will be gradually slower with the proceeding of constant voltage charge due to potential difference contraction between the charging voltage and open circuit voltage of the battery. At  $t=14s$ , the discharge state is started which causes the decrease of SOC between  $t=14$  and  $t=20$  as shown in Fig. 7.2a.

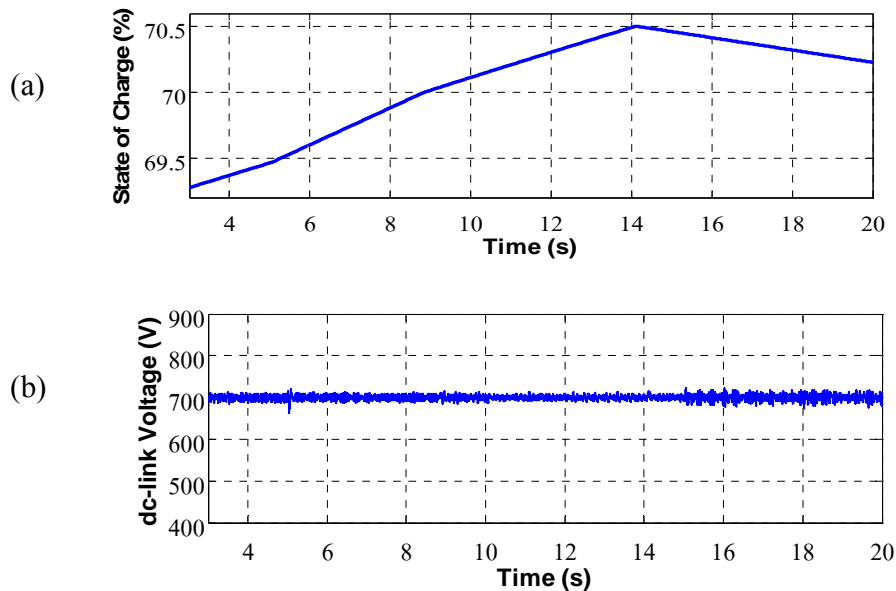


Fig. 7.2 State of Charge and DC-Link voltage during the charge/discharging and reactive power control

In the entire charging and discharging process, all the parameters work under expected condition. Even the biggest oscillation caused by the switch between constant current and constant voltage charging status (figure 7.1) is also under the satisfactory range. Meanwhile, the DC-Link voltage is maintained at the expected value of 700V which shows a good stability (figure 7.2b).

In terms of grid reactive power control, variable reference values of reactive power are applied during the charging and discharging process. In figure 7.3a, the q-axis current reference

of the GSC controller is set to zero at the beginning so that no reactive power is absorbed from the grid before  $t=5$ . Then, the reactive power reference is set into 200KVar, 300Kvar and 50Kvar in sequence after  $t=5$  and the net reactive power at the PCC is totally maintained at the reactive power reference. On the other hand, because of the relativity between  $I_q$  and reactive power, the q-axis current always follows the reactive power control command while the grid d-axis current changes slightly depending on the charging and discharging speed of the battery as shown in Fig 7.3b.

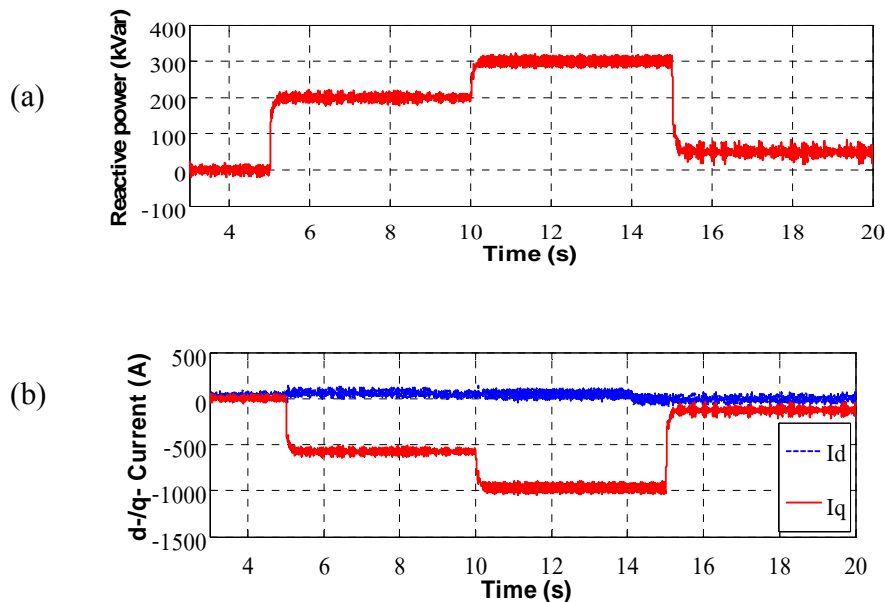


Fig. 7.3 Reactive power control

### 7.1.2 Charge/Discharge and Grid Voltage Support Controls

In battery and grid voltage support control mode, both d- and q-axis current references of the GSC controller are variable, making  $|v_{dq1}^*|$  generated by the controller more possible to go over the converter linear modulation limit. Using the direct-current vector control configuration, the PI coefficients of the current-loop controller remain unchanged, showing superior adaptability of the direct-current control mechanism to different control conditions.

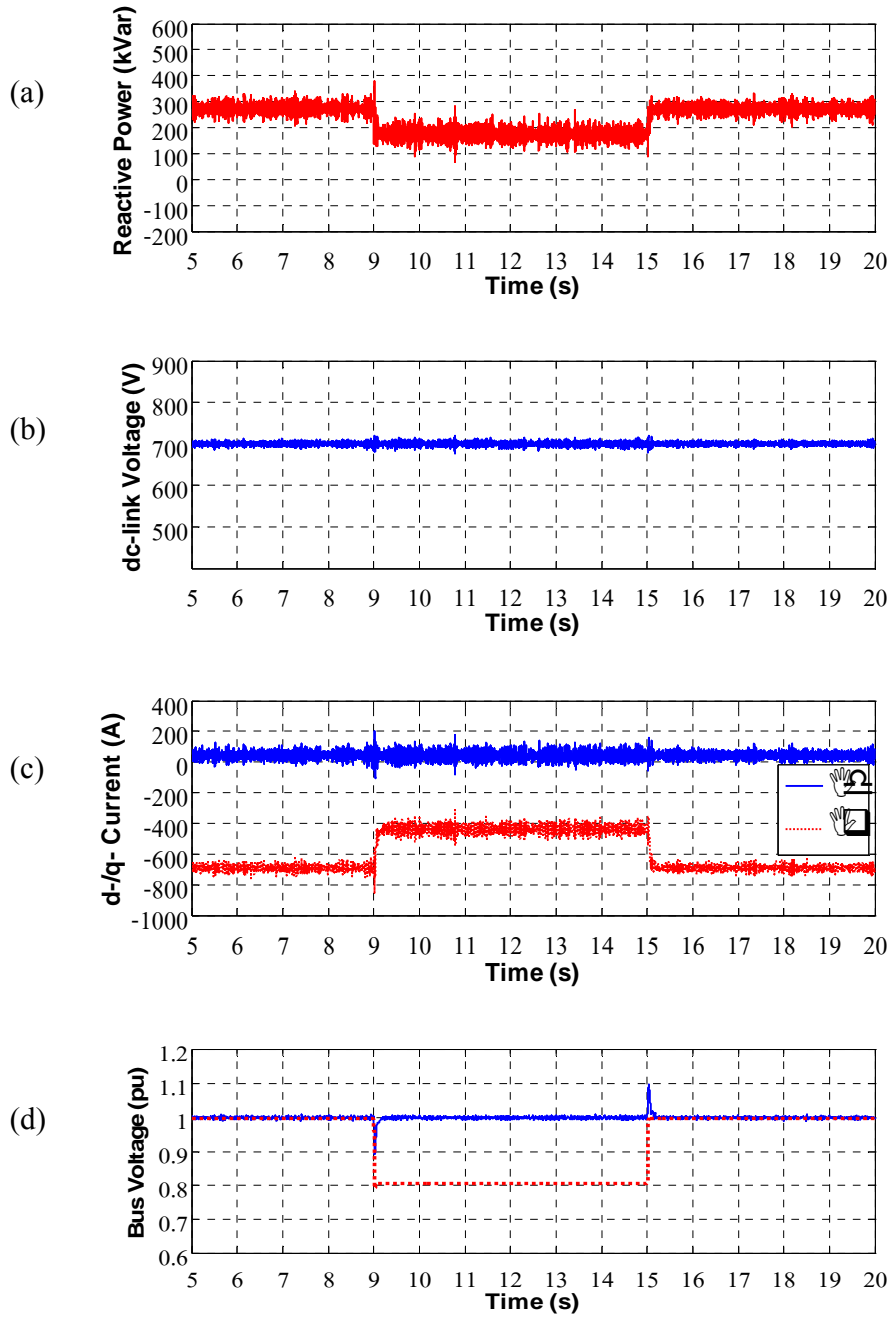


Fig. 7.4 GSC and ESC for battery and grid voltage support controls

Figure 7.4 presents a PCC voltage support control study for a voltage sag condition, in which a voltage droop is generated between 9s and 15s. The reactive power is in general absorbed due to a capacitor between the PCC and the grid. For the voltage sag on the PCC bus,

the GSC under the direct-current vector control works properly for dc-link voltage and PCC bus voltage support control (figures 7.4b and 7.4d). At the start of the voltage sag, there is a sudden decrease of PCC bus voltage (figure.7.4d). But, the GSC under the direct-current vector control configuration quickly recovers the PCC bus voltage to the rated value and stabilizes the dc-link voltage at the reference value. During the voltage support control mode, the GSC, operating as a STATCOM, reduces the absorbing reactive power and increases  $q$ -axis current  $i_q$  until the rated current or linear modulation constraint of the GSC is reached (figure. 7.4d). When the voltage sag is cleared at  $t=15s$ , there is another oscillation of the PCC voltage. Again, the GSC under the direct-current vector control configuration quickly recovers the system to the normal operation.

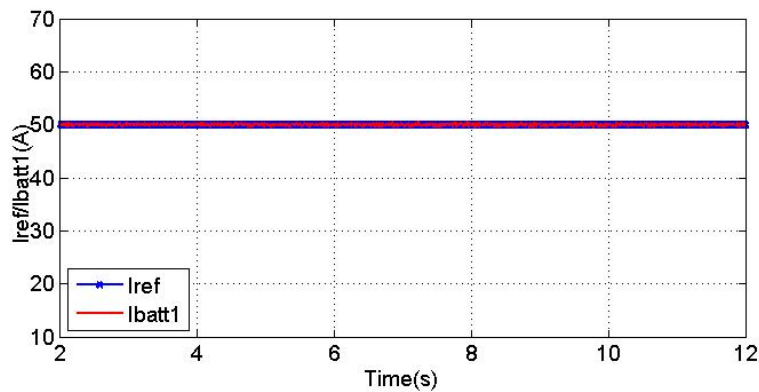
## **7.2 G2V, V2G and V2V simulation**

The purpose of the simulation in this section is to test the performance of the integrated EDVs charging station in G2V, V2G and V2V functions. Different from the case study shown in Section 7.1 with only one EDV, three EDVs are equipped to make aforementioned operations available. With the DC bus established by the GSC, the power direction of each EDV connected with the charging station can be easily controlled by sending a control signal to the corresponding DC-DC converters. Similar to the simulation in the previous section, the charging scheme is still utilizing CC/CV charging strategy while the discharging process is under a stable rated current.

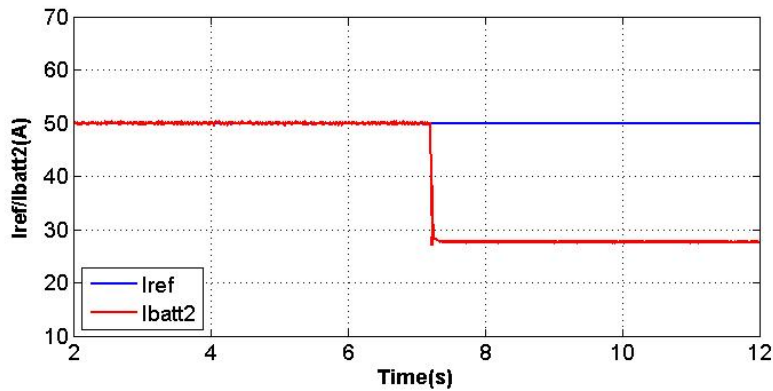
### **7.2.1 G2V model simulation**

In G2V model, every EDV works under charging model and power is transferred from grid side to EDVs side. The batteries of three EDVs are set with different SOC to make each battery charged under different charging stage of constant current/constant voltage charging

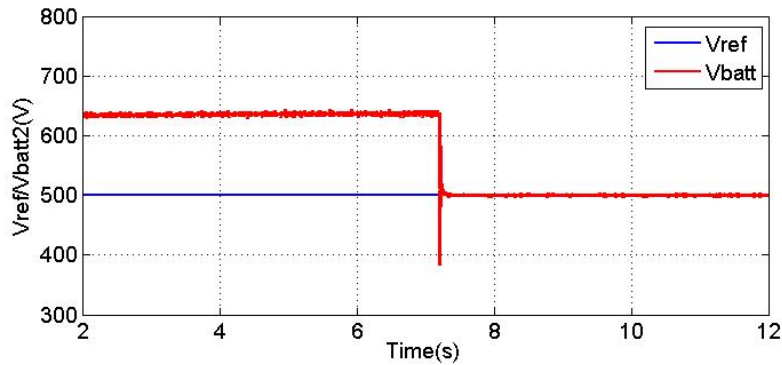
scheme in 12 seconds simulation period as shown in figure 7.5. For the first battery, the SOC is set as 30% and the battery is charged by constant current in the entire simulation process (figure. 7.5a). In the case of the second battery, the SOC is a little bit lower than 70% at the beginning of the charging simulation. Therefore, there will be a switch between constant current charge and constant voltage charge when the battery SOC reaches 70% around  $t=7s$  (figures. 7.5b and 7.5c). Meanwhile, the SOC of the third battery is set higher than 70% which means the constant voltage charging stage is operated in 12 seconds simulation (figure 7.5d).



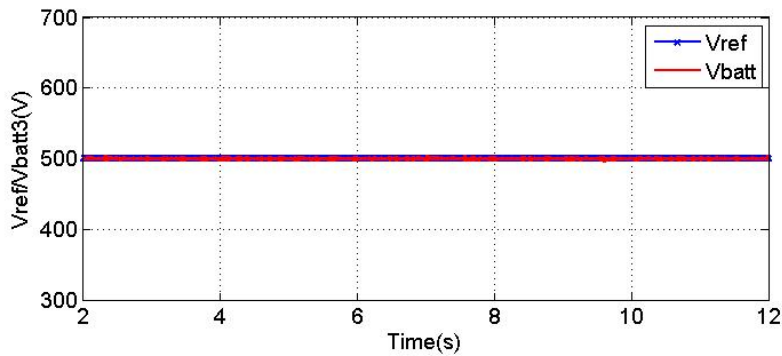
a) Current reference and measured current of the EDV1 in the G2V mode



b) Current reference and measured current of the EDV2 in the G2V mode



c) Voltage reference and measured voltage of the EDV2 in G2V mode



d) Voltage reference and measured voltage of the EDV3 in G2V mode

Fig. 7.5. Charging scheme for G2V mode

Figure 7.6 illustrates real/reactive power and DC-Link voltage results in G2V model simulation. Since all the EDVs are absorbing power from grid side, the real power of the charging station keeps in a positive level as shown in figure. 7.6a. In addition, there is a drop of real power around  $t=7s$  when the second battery transfers from constant current charging scheme to constant voltage charging scheme. This drop indicates that less power is obtained by battery in constant voltage charge than constant current charge scheme, which can help to prevent battery from overcharge and overheat problems. On the other hand, for the purpose of compensating the voltage in PCC, the reactive power is around 450kVar which is much higher than the real power. Moreover, the DC-Link voltage sustains at 700V throughout the simulation period which shows well stability (figure. 7.6b).

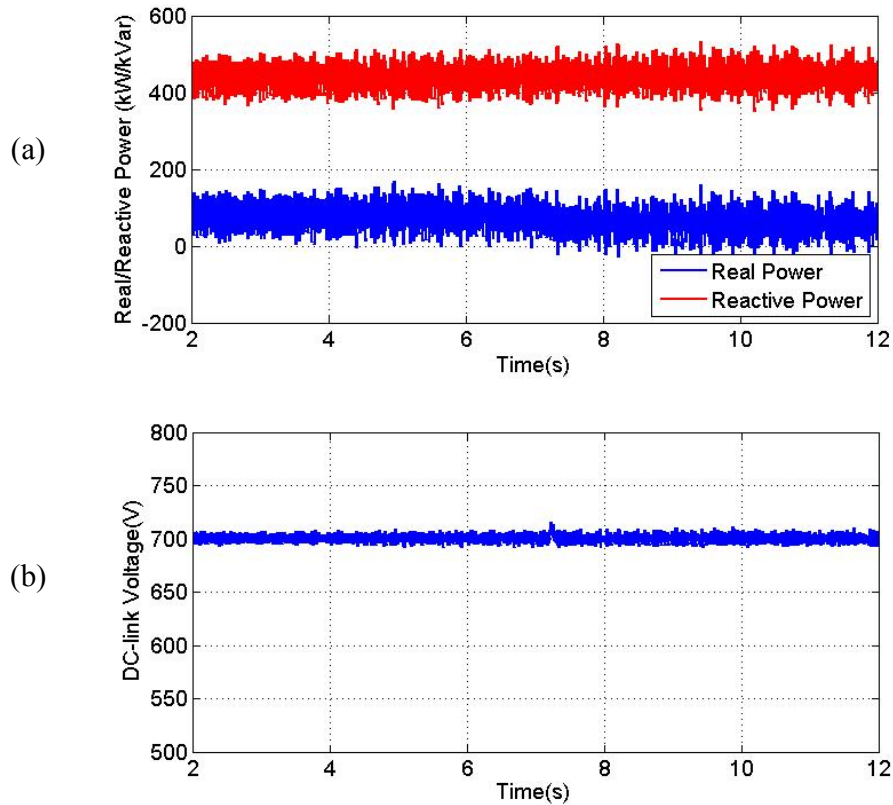


Fig. 7.6 Real/Reactive power and DC-Link voltage for G2V mode

### 7.2.2 V2G model simulation

In the V2G mode, all the EDVs are discharged in a constant current and the power is transferred from the EDVs side to grid side. Figure 7.7 presents the discharging current reference and measured discharging current. It is clear that the actual discharging current fully follows the discharging current reference which is 30A in this thesis. The simulating result of real and reactive power is illustrated in figure 7.8. Similar as the G2V model, the reactive power is still keeping around 400kVar for the purpose of PCC voltage compensation. The measured real power is a negative value in V2G model due to the reason that the power flowing direction is from EDV side to Grid side. Because the discharging current is relative small while the oscillation of power is very large, the negative power value is hardly distinguished in the figure

7.8. Moreover, the DC-Link voltage still stabilizes at the 700V in the entire simulating process as shown in figure 7.9.

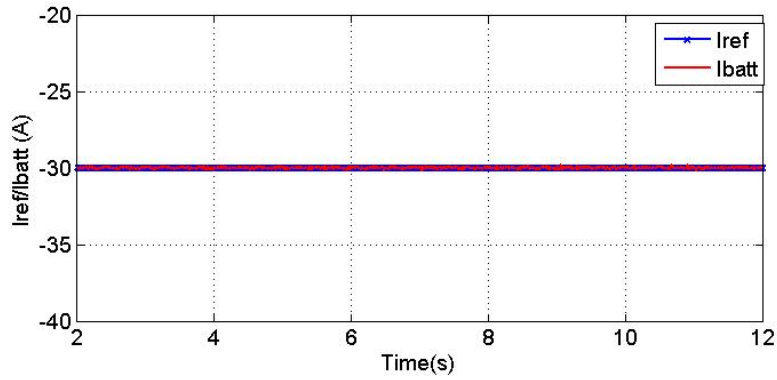


Fig. 7.7 Discharging current for V2G mode

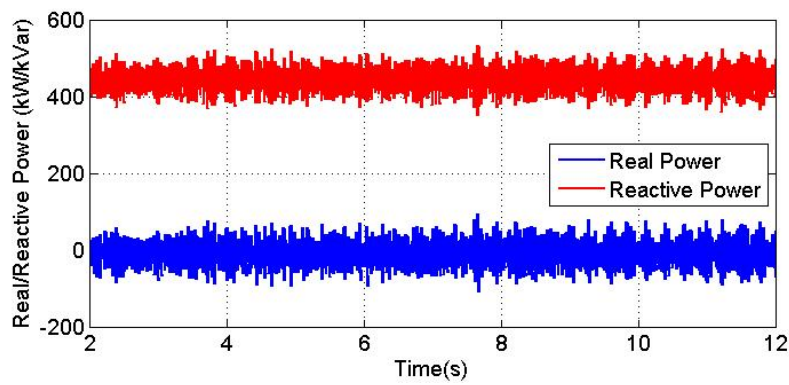


Fig. 7.8 Real power and reactive power for V2G mode

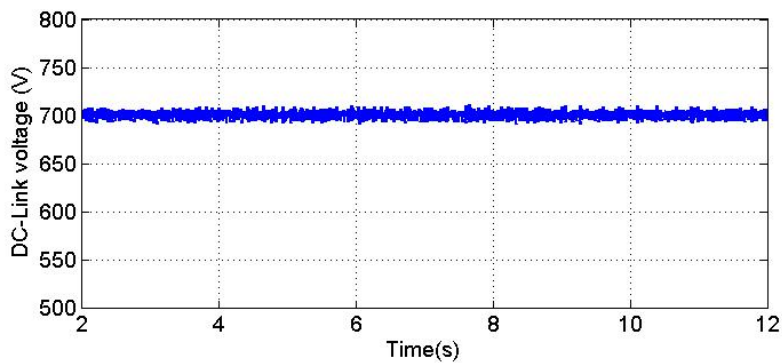


Fig. 7.9 DC-Link voltage for V2G mode

### 7.2.3 V2V model simulation

The V2V model stands for the function that power just flowing between the EDVs in which the grid does not switch power with EDV side. To realize this model, two EDVs are discharged in constant current while the other EDV is obtaining power from them. The specific charging and discharging schemes are the same as section 7.2.1 and section 7.2.2 and are shown in figure.7.5 and figure.7.7. Figure.7.10 presents the power of the charging battery where the fall of power around  $t=7s$  is caused by the switch between constant current charge and constant voltage charge. The real power between grid side and EDV side of the EDVs charging station is illustrated in figure 7.11. Since the power provided by the two discharging EDVs is probably able to satisfy demand of the battery that is charged, the real power between Grid side and EDV side is equal to zero.

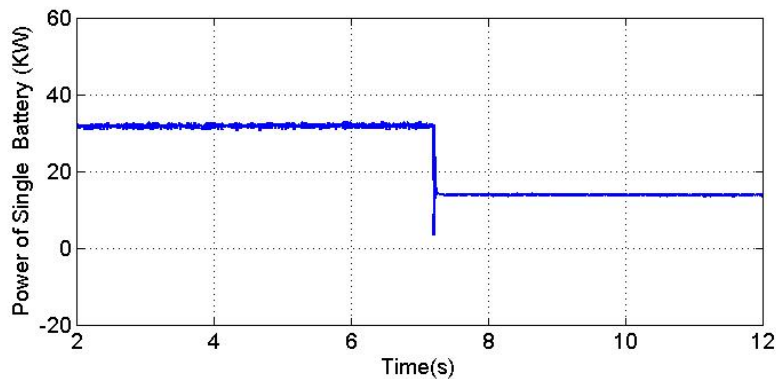


Fig.7.10 Power of the charged battery

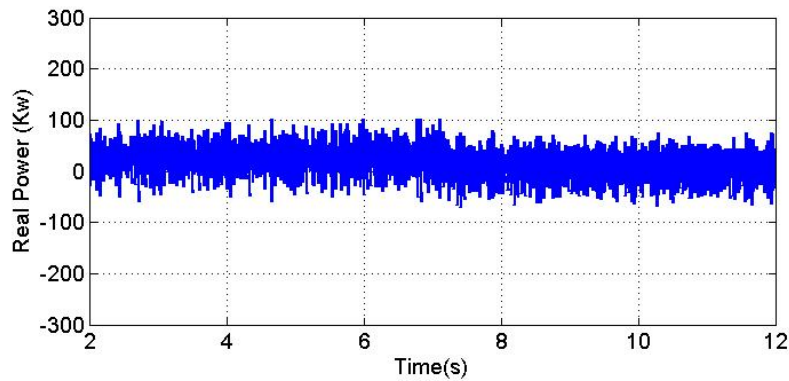


Fig.7.11 Real Power from grid side to EDVs side for V2V mode

### 7.3 Conclusions

The real-time simulation of the EDVs charging station shows the performance of the proposed control techniques. For the proposed control mechanism, the results demonstrate that it can work properly in both grid-side control and EDVs side control schemes no matter how the external conditions vary. The DC link voltage can be stable at the expected value even for extreme conditions. The reactive power output of the systems can also be controlled effectively when the reactive power control is operated in the grid side system. In addition, the V2G, G2V and V2V mode is achieved separately through the EDVs side control strategies. By setting the references of the EDVs side controller; it is simple to operate each of EDVs under expected functions such as CC/CV charging operation or constant current discharging operation. According to the results of the real-time simulation, the proposed charging current, charging voltage and discharging current are also under the acceptable oscillation range.

## CHAPTER 8

### SUMMARY AND FUTURE WORK

The next decade will bring a significant shift toward the electrification of transportation around the globe. This development trend will fundamentally change how electric utilities do business and strain their existing infrastructure. This thesis presents an energy control study in a charging station, a typical integrated EDV and utility system. The charging station consists of an AC/DC converter for grid interface and multiple DC/DC converters for EDV battery management. A direct-current control mechanism for grid-side converter is employed for reactive power, AC system bus voltage, and DC-link voltage control, which has demonstrated superior performance for EDV battery management. For the EDV-side converters, constant-current and constant voltage control mechanisms are investigated for charge and discharge control to implement V2G and G2V energy management requirements in a dynamic price framework.

Comprehensive simulation studies demonstrate that the overall charging station control structure can effectively accomplish integrated electric vehicle and utility interface control objectives with superior performance under both steady and variable charging and discharging conditions within the physical constraints of power converters. Beyond physical constraints of power converters, the proposed control approach operates the system by regulating the ESC within its rated range and by controlling the GSC to stabilize the dc-link voltage as the main concern.

For the future work, some more intelligent control approaches are necessary to be improved to endow other capabilities to the integrated EDVs charging station. First, many functions of the charging station are based on the information from the battery models, such as SOC, batter charging /discharging voltage and current. Unlike the thesis directly receives these information from the battery model, it is complicated to measure them accurately in reality. Therefore, a battery manage system (BMS) is still required for the EDVs charging station. Second, the V2G, G2V and V2V functions are three attractive capabilities of the charging station in this thesis. Because the operation of these three functions depends on the fluctuation of the dynamic electricity price, the corresponding power management strategy needs to be improved in order to realize the intelligent power management in the future smart grid.

## REFERENCES

- 1) Morrow, K., Karner, D., & Francfort, J. (2008). Plug-in Hybrid Electric Vehicle Charging Infrastructure Review. Retrieved September 13, 2011, from <http://avt.inel.gov/pdf/phev/phevInfrastructureReport08.pdf>
- 2) Wirasingha, S. G., Schofield, N., & Emadi, A. (2008). Plug-in hybrid electric vehicle developments in the US: trends, barriers, and economic feasibility. IEEE Vehicle Power and Propulsion Conference, 2007. VPPC 2007, pp. 1-8, Sept. 2008.
- 3) Burke, A.F. (2007). Batteries and Ultracapacitors for Electric, Hybrid, and Fuel Cell Vehicles. Proceedings of the IEEE, vol. 95, issue 4, pp. 802-820, April. 2007.
- 4) Divya, K.C., & Østergaard, J. (2009). Battery energy storage technology for power systems—An overview, Electric Power Systems Research, 79, 511–520.
- 5) Barton, J.P., & Infield, D.G. (2004). Energy Storage and Its Use with Intermittent Renewable Energy, IEEE Transactions on Energy Conversion, vol. 19, issue 2, pp. 441 – 448, June 2004.
- 6) Wang, Q., Lin, C., Yang, X., & Liu, J.(2010), Scheme of intelligent community based on distributed generation and micro-grid, Power System Technology (POWERCON), 2010 International Conference, 1-6 ,Issue Date: 24-28 Oct. 2010, Hangzhou.
- 7) Sanzhong, B., Yu, D., & Lukic, S. (2010). Optimum design of an EV/PHEV charging station with DC bus and storage system, Energy Conversion Congress and Exposition (ECCE), 2010. IEEE, pp. 1178-1184, 12-16 Sept. 2010.
- 8) Nursebo, S. (2010). Model Based Approach to Supervision of Fast Charging. Retrieved Oct 18, 2011, from Chalmers University of Technology. Web site: <http://webfiles.portal.chalmers.se/et/MSc/ShemsedinNursebo.pdf>
- 9) Rajapakse, A., Muthumuni, D., & Perera, N. (2011). Grid Integration of renewable energy systems. Retrieved August 3, 2011, from [http://cdn.intechopen.com/pdfs/9325/InTech-Grid\\_integration\\_of\\_renewable\\_energy\\_systems.pdf](http://cdn.intechopen.com/pdfs/9325/InTech-Grid_integration_of_renewable_energy_systems.pdf)

- 10) Ghatikar, G., Mathieu, J.L., Piette, M.A., Koch, E. & Hennage, D. (2010). Open Automated Demand Response Dynamic Pricing Technologies and Demonstration. Retrieved May 18, 2011, from Lawrence Berkeley National Laboratory, June 2010.
- 11) Pumping and Agricultural Real-Time Pricing. (2010). Retrieved August 13,2011, from Southern California Edison, website: [http://asset.sce.com/Documents/Business%20-%20Rates/PA\\_RTP\\_FactSheet.pdf](http://asset.sce.com/Documents/Business%20-%20Rates/PA_RTP_FactSheet.pdf)
- 12) Salameh, Z. M., Casacca, M. A., & Lynch, W. A.(1992). A mathematical model for lead-acid batteries, IEEE Trans. Energy Conversion, vol. 7, no. 1, pp. 93–98, Mar. 1992
- 13) Chen, M. and Rincon-Mora, G.A. (2006), Accurate Electrical Battery Model Capable of Predicting Runtime and I–V Performance,” IEEE Trans. Energy Conversion., vol. 21, no. 2, pp. 504-511, June 2006.
- 14) Salameh, Z. M., Casacca, M. A. & Lynch, W. A. (1992). A mathematical model for lead-acid batteries, IEEE Trans. Energy Conversion, vol. 7, no. 1, pp. 93–98, Mar. 1992.
- 15) Valvo, M., Wicks, F. E., Robertson, D., & Rudin, S. (1996). Development and application of an improved equivalent circuit model of a lead acid battery. In Proc. Energy Convers. Eng. Conf., vol. 2, pp. 1159–1163, Aug. 1996.
- 16) Ceraolo M. (2000), New dynamical models of lead-acid batteries. IEEE Trans. on Power Systems, vol. 15, no. 4, pp. 1184–1190, Nov. 2000.
- 17) Barsali, S. and Ceraolo, M. (2002). Dynamical models of lead-acid batteries: Implementation issues. IEEE Trans. Energy Conversion, vol. 17, no. 1, pp. 16–23, Mar. 2002.
- 18) Benini, L., Castelli, G., Macci, A., Macci, E., Poncino, M., & R. Scarsi. (2001) Discrete-time battery models for system-level low-power design. IEEE Trans. Energy Conversion, vol. 9, no. 5, pp. 630–640, Oct. 2001.
- 19) Schweighofer, B., Raab, K. M., & Brasseur, G. (2003). Modeling of high power automotive batteries by the use of an automated test system. IEEE Trans. on Instrument Measurement, vol. 52, no. 4, pp. 1087–1091, Aug. 2003.
- 20) Gao, L., Liu, S. & Dougal, R. A. (2002). Dynamic lithium-ion battery model for system simulation. IEEE Trans. Compon. Packag. Technol., vol. 25, no. 3, pp. 495–505, Sep. 2002.

- 21) Buller, S., Thele, M. R., Doncker, W. D., & Karden, E. (2005). Impedance based simulation models of supercapacitors and Li-ion batteries for power electronic applications. *IEEE Transactions on Industry Applications*, Vol. 41, Issue 3, pp. 742 – 747, May-June 2005,.
- 22) Baudry, P., Neri, M., Gueguen, M., & Lonchamp, G. (1995). Electro-thermal modeling of polymer lithium batteries for starting period and pulse power. *J. Power Sources*, vol. 54, no. 2, pp. 393–396, Apr. 1995.
- 23) Zhang, H. & Mo-Yuen Chow. (2010). Comprehensive Dynamic Battery Modeling for PHEV Applications. *Proceedings of 2010 IEEE PES General Meeting, Minneapolis, MN, July 26-29, 2010.*
- 24) Dell, R. & Rand, D.A.J. (2001). *Understanding batteries*. Royal Society of Chemistry.
- 25) Linden, D. and Reddy, T.B. (2001). *Handbook of Batteries* (3rd ed). McGraw-Hill. 2001.
- 26) Tremblay, O. & Dessaint, L.A. (2009). Experimental Validation of a Battery Dynamic Model for EV Applications. *World Electric Vehicle Journal*, 3, 2032-6653.
- 27) Bindner, H., Cronin, T., Lundsager, P., Manwell, J.F., Abdulwahid, U. & Baring-Gould, I. (2005). Lifetime Modelling of Lead Acid Batteries. Retrived May 18, 2010, from Risø National Laboratory, Roskilde, Denmark.
- 28) Feng, X. & Sun, Z. (2008). A battery model including hysteresis for State-of- Charge estimation in Ni-MH battery. *Proceedings of Vehicle Power and Propulsion Conference, 2008. VPPC '08. IEEE*, pp. 1-5.
- 29) Dickerman L. & Harrison J. (2010). A New Car, a New Grid. *IEEE Power & Energy Magazine*, Vol. 8, Issue. 3, 55-61, March/April 2010.
- 30) Ling, X. (2009). Control of Power Converter for Grid Integration of Renewable Energy Conversion and Statcom Systems. Retrieved August 30 2011, from The University of Alabama.
- 31) Liserre, M. & Hansen. S. (2005). Design and Control of an LCL-Filter-Based Three-Phase Active Rectifier. *IEEE Transactions on Industry Applications*, vol. 41, no.5, pp. 1281-1291.
- 32) Bojrup, M., Karlsson, P., Alakula, M. & Simonsson, B. A Dual Purpose Battery Charger for

Electric Vehicles. Retrieved November. 15<sup>th</sup>, 2011, from Department of Industrial Electrical Engineering and AutomationLund Institute of Technology. Website: <http://www.iea.lth.se/~ielper/charger/PESC98-paper.pdf>

- 33) Liserre, M., Blaabjerg, F., & A. Dell'Aquila. (2004) Step-by-step design procedure for a grid-connected three-phase PWM Voltage Source Converter. *Int. J. Electron.*, vol. 91, no. 8, pp. 445–460.
- 34) Blasko, V. & Kaura, V. (1997) A novel control to actively damp resonance in input LC filter of a three-phase voltage source converter. *IEEE Trans. Ind. Appl.*, vol. 33, no. 2, pp. 542–550.
- 35) Twining, E. and Holmes, D. G. (2002). Grid current regulation of a three-phase voltage source inverter with an LCL input filter. *Proc. IEEE PESC'02*, vol. 3, Jun. 2002, pp. 1189–1194.
- 36) Li, S., & Haskew T.A. (2007). Analysis of decoupled d–q vector control in DFIG back-to-back PWM converter. *Proceedings of IEEE Power Engineering Society 2007 General Meeting*, Tampa FL, June 24–28.
- 37) Li, S., Haskew, T. A., Hong Y & Xu. L. (2011). Direct-current vector control of three-phase grid-connected rectifier–inverter. *Journal of Electric Power Systems Research*, 81, 357-366.
- 38) Field oriented control of 3-phase AC-Motors. Available: <http://focus.ti.com/lit/an/bpra073/bpra073.pdf>
- 39) Affanni, A., Bellini, A., Franceschini, G., Guglielmi, P., & Tassoni, C. (2005). Battery Choice and Management for New-Generation Electric Vehicles. *IEEE Transactions on Industrial Electronics*, vol. 52, pp. 1343-1349.
- 40) Srinivasaraghavan, S. & Khaligh, A. (2011) Time Management. *Power and Energy Magazine*, IEEE, Vol. 9, Issue. 4, 46-53, July/Aug. 2011.
- 41) Wang, Q., Lin, C., Yang, X., & Liu, J. Scheme of intelligent community based on distributed generation and micro-grid. *Power System Technology (POWERCON)*, 2010 International Conference, 1-6, issue: 24-28 Oct. 2010, Hangzhou.
- 42) Wang, J., Cao, B., Chen. Q., & Wang, F.. (2007). Combined state of charge estimator for electric vehicle battery pack. *Control Engineering Practice*. Volume 15, issue 12, 1569-1576, December 2007.

- 43) Erol-Kantarci, M., Mouftah, H.T. (2011). Management of PHEV batteries in the smart grid: Towards a cyber-physical power infrastructure, in proceeding of Wireless Communications and Mobile Computing Conference (IWCMC), Istanbul, Turkey, July. 5-8, 2011.
- 44) Bojrup, M. (1999). Advanced Control of Active Filters in a Battery Charger Application. Retrieved October 14, 2011, from Department of Industrial Electrical Engineering and Automation (IEA), Lund Institute of Technology (LTH).
- 45) Dufour, C., Andrade, C. & Bélanger, J., Real-Time Simulation Technologies in Education: a Link to Modern Engineering Methods and Practices. Retrieved March 3, 2012, from: <http://www.opal-rt.com/technical-document/real-time-simulation-technologies-education-link-modern-engineering-methods-and>
- 46) Bélanger, J., Venne, P., & Paquin, J. The What, Where and Why of Real-Time Simulation. Retrieved March 9, 2012, from: [http://www.opal-rt.com/sites/default/files/technical\\_papers/PES-GM-Tutorial\\_04%20-%20Real%20Time%20Simulation.pdf](http://www.opal-rt.com/sites/default/files/technical_papers/PES-GM-Tutorial_04%20-%20Real%20Time%20Simulation.pdf)
- 47) Banks, J., Carson, J., Nelson, B. & Nicol D. (2001). Discrete-Event System Simulation. (3rd ed.). Prentice Hall.
- 48) RT-Lab Quick Guide. Retrieved March 15, 2012, from: <http://www.opal-rt.com/>
- 49) Artemis Guide. Retrieved March 15, 2012, from: <http://www.opal-rt.com/>
- 50) RT-Event Guide. Retrieved March 15, 2012, from: <http://www.opal-rt.com/>